Platinum-catalyzed Nb–doped TiO_2 and Nb-doped TiO_2 nanotubes for hydrogen generation in proton exchange membrane water electrolyzers

Francisco Alcaide[a], Radostina V. Genova[a,b], Garbiñe Álvarez[a], Hans-Jürgen Grande[a], Óscar Miguel[a], Pere L. Cabot[b,*]

[a]*CIDETEC, Paseo Miramón, 196, 20014 Donostia-San Sebastián, Spain.*

[b]*Laboratory of Electrochemistry of Materials and the Environment, Dept. of Materials Science and Physical Chemistry, Faculty of Chemistry, Universitat de Barcelona, Martí i Franquès, 1-11, 08028 Barcelona, Spain.*

*Author for correspondence: Tel: (+34) 934039236, Fax: (+34) 934021221, E-mail: p.cabot@ub.edu (Pere L. Cabot).

ABSTRACT

This paper studies the catalytic activity of Pt deposited onto Nb-doped titania supports toward the hydrogen evolution reaction (HER). New catalysts based on Nb-doped TiO_2 nanoparticles (*n*Nb-TiO_2) and Nb-doped TiO_2 nanotubes (*n*Nb-TNTs), with *n* in the range 3-10 at % (Nb+Ti), were synthesized. The specific surface areas of *n*Nb-TNTs were 250−300 m^2g^{-1}, about three times higher than those of *n*Nb-TiO_2. X-ray diffraction showed the Nb incorporation into the TiO_2 lattice with its consequent lattice expansion. The X-ray photoelectron spectra of Pt deposited onto Nb-doped titania revealed a negative charge accumulation on Pt, thus denoting strong metal-support interaction. The electrochemical characterization in acidic media showed that Pt supported on *n*Nb-TiO_2 and *n*Nb-TNTs presented better activity towards the HER than that of Pt deposited onto the un-doped supports and commercial Pt on carbon. The best performance was obtained with a small Nb doping of 3 at %.

Keywords: Hydrogen evolution reaction; TiO_2 supports; TiO_2 nanotubes; Nb doping; Pt catalyst; PEMWE.

1. Introduction

Within the last years, there is a renewed interest in the H_2 production from polymer electrolyte membrane water electrolyzers (PEMWEs). It is considered to be one of the most promising forms to produce high purity and fossil-free H_2 from renewable energy sources [1-5]. The most effective electrocatalysts for the hydrogen evolution reaction (HER) have been proven to be those based on Pt. However, the high cost and scarcity of Pt are a drawback in the development of large-scale applications [6]. For this reason, reducing the amount of Pt and developing Pt-free catalysts have been examined [2-13]. However, performance, corrosion resistance, mechanical stability and durability, as long as reducing the cost, are essential for the technical electrodes in PEMWEs.

The Pt loading could be reduced by improving the catalyst dispersion on high specific surface area supports and/or developing Pt-based alloys. Among the Pt-free catalysts, MoS_x- and Pd-based nanocarbons have shown reasonable good electroactivity and stability [3]. Using high specific surface area supports alternative to carbon is particularly interesting, because it allows avoiding the drawbacks associated to the use of carbon in terms of durability and performance. The H_2 and O_2 permeation between cathode and anode through the membranes of the PEMWEs has been demonstrated [14-16] and although O_2 permeation is slower than that of H_2, it increases with current density and temperature (as H_2 permeation does). The O_2 content in the H_2 product was found to be 3-4 times greater when using Pt-free instead of Pt cathode catalysts [15]. It has also been reported that the presence of O_2 at the cathode can lead to the formation of hydrogen peroxide and hydroxyl radicals, which can produce membrane and carbon degradation especially when turning off [16]. Therefore, it is interesting to explore non-carbonaceous supports with high specific surface area.

It is well known that TiO_2 has very good chemical resistance and thermal stability and has been widely investigated for different applications such as in photocatalysis and sensors [17-22]. It has also been investigated as support for Pd [23] and Pt catalysts in fuel cells [24-27] and its higher durability and stability in comparison to the conventional carbon support have been proved. Shim et al [24] studied the electrochemical performance of Pt-TiO_2/C toward the hydrogen oxidation and to the oxygen reduction in fuel cells. They explained the better performance with respect to Pt/C by an electrochemical active surface area (ECSA) increase and a lower adsorption strength of hydrogen and oxygen onto the Pt of Pt-TiO_2. Xiong and Manthiram [25], in a direct methanol fuel cell, assigned the enhanced catalytic activity of Pt/TiO_2/C toward the oxygen reduction to the increased ECSA and modified surface electronic properties of Pt. Gustavsson et al [26] attributed the better catalytic activity of Pt/TiO_2 toward the oxygen reduction reaction in comparison to Pt-black, to the better dispersion of Pt onto the oxide surface and to the substantial proton conduction of TiO_2 when a thin layer of the latter was placed between the Nafion membrane and Pt. Lewera et al [27] reported, from X-ray photoelectron spectroscopy (XPS) analyses, changes in the electronic properties of Pt deposited on a TiO_2/C composite with respect to Pt/C, induced by a strong metal-support interaction (SMSI), which was explained by the formation of a surface Pt-Ti alloy and/or a partial charge transfer from TiO_2 to Pt. This partial charge transfer would explain the reported enhanced electrocatalytic activity toward the oxygen reduction in the fuel cell cathode.

The TiO_2 conductivity is low [1,17,28,29]. However, with Nb doping, its conductivity increases by three orders of magnitude [29]. The ionic radii of Nb^{5+} and of Ti^{4+} have approximately the same size, 0.70 and 0.68 Å, respectively, thus allowing obtaining a solid solution of the former in TiO_2 [30-34]. The conductivity increase is explained by

the effect of Nb ions in providing electrons with energy levels in the TiO_2 bandgap that can be excited to the conduction band [35]. Nb-doped TiO_2 has also been satisfactorily tested as support for Pt in proton exchange membrane fuel cells (PEMFCs) [30,33,34,36,37]. Apart from increasing the TiO_2 conductivity, Nb doping allowed obtaining Nb-TiO_2 supports with greater specific surface area than that of TiO_2, thus allowing a better catalyst dispersion. Thus, Gojković et al [34] claimed that Pt/Nb-TiO_2 were promising high area supports for PEMFC anodes. Chhina et al [30] and Chevallier et al [37] found better stability for the Pt/Nb-TiO_2 catalysts than for Pt/C despite the later gave initially slight better performance. Elezović et al [33] tested the Pt/Nb-TiO_2 nanocatalyst for the oxygen reduction, finding a higher activity and methanol tolerance than Pt/C. Similar results for the oxygen reduction were found for Do et al [36]. For these supports, specific surface areas in the range from 72 [33,34] to 150 $m^2\ g^{-1}$ [37] were reported.

On the other hand, Nb-doped TiO_2 supports for IrO_2 toward the oxygen evolution reaction in PEMWEs have been developed with satisfactory results [29,38,39]. Hu et al [38] prepared by means a sol-gel process a corrosion-resistant $Nb_{0.05}Ti_{0.95}O_2$ support of 83 $m^2\ g^{-1}$. Hao et al [29] obtained mesoporous Nb(5-20 at %)-doped TiO_2 with surface areas up to 146.5 $m^2\ g^{-1}$ by means of the modified evaporation-induced self-assembly method. Recently, we have prepared titania nanotubes (TNTs) doped with 3 at % Nb (3Nb-TNTs) with a surface area of 260 $m^2\ g^{-1}$ [39], which is comparable to that of Vulcan XC72 of about 250 $m^2\ g^{-1}$. It was found that the oxygen evolution reaction activity after supporting IrO_2 and IrRuOx increased with Nb doping [29,39]. This was explained by the surface area increase with respect to that of pristine titania, which allowed a good catalyst dispersion and accessibility, and to the ability in transferring charge of the niobium oxide

species. The stability of the Nb-doped TiO_2-supports was also shown to be better than that of unsupported IrO_2 [29].

The Pt/TiO_2 catalyst for the HER has been scarcely studied in the literature, although with promising results [40]. Thus, Pt nanoparticles supported on nitrogen-doped black TiO_2 (Pt/N_x:TiO_{2-x}) showed robust durability and onset potentials for the HER, which were somewhat smaller than that of commercial Pt/C catalyst. To the best of authors' knowledge, Nb-doped TiO_2 and TNTs have not yet been reported to be used as Pt supports for the HER. There are, however, a number of recent papers dealing with the use of Pt-free catalysts supported on TiO_2 for the HER in both, acidic [41-49] and alkaline [49-53] electrolytes. Different catalysts such as quantum dots, IrO_2 and MoS_x, Ni, Ru and Co species, were supported on nanostructured and mesoporous TiO_2 [46-49,51-53] and on TNT arrays produced by Ti anodizing [41-45,50]. The TiO_2 used was generally non-doped, although a fast electron transfer was reported for N-doped TNTs [44]. The stability results were good, although the electroactivity of such Pt-free catalysts were generally still lower than that of Pt/C. It is worth to note the exception of the porous Pd-CN_x composite [54], which needed an overpotential of only -0.055 V to reach 10 mA cm^{-2}, in front of a value of -0.058 V for commercial Pt/C.

Considering all the points discussed above, i.e. carbon degradation and good performance of Nb-doped TiO_2 as the anode catalyst support both, for the oxygen evolution in PEMWEs and for the H_2 oxidation in PEMFCs, it is justified studying Pt supported on Nb-doped TiO_2 and TNTs as catalysts for the HER in PEMWEs. In this paper, different Pt catalysts supported on TiO_2 and Nb-doped TiO_2, TNTs, and Nb-doped TNTs were synthesized and tested for the HER in acidic media. Nb-doped TiO_2 and TNTs were prepared by the sol-gel and modified hydrothermal techniques, respectively. Different Nb concentrations in the range 0-10 at % toward the overall amount of Nb+Ti

in TiO_2 and TNTs were investigated. Their morphological, textural and compositional properties were determined using scanning electron microscopy (SEM), transmission electron microscopy (TEM), N_2 adsorption/desorption isotherms, X-ray diffraction (XRD), XPS, and their electrochemical performance by means of cyclic voltammetry (CV) and linear sweep voltammetry (LSV). The catalytic performance of such electrocatalysts toward the HER was compared to previous results in the literature.

2. Experimental

2.1. Synthesis of the supports and Pt electrocatalysts

All reactants used in the synthesis of materials were reagent grade. Ultrapure water ($\kappa \leq$ 0.054 μS cm^{-1}) was obtained from Millipore System Simplicity 185.

The sol-gel technique was applied for the synthesis of TiO_2 and Nb-doped TiO_2, the latter with 3, 6, and 10 at % Nb, being respectively denoted as 3Nb-TiO_2, 6Nb-TiO_2, and 10Nb-TiO_2. Titanium (IV) n-butoxide (98 %, Alfa Aesar) and niobium (V) ethoxide (99.999 %, Alfa Aesar) were mixed in absolute ethanol media (0.20 mol dm^{-3} in Nb ethoxide) in the appropriate stoichiometric ratio. Then, hydrochloric acid (37 %, Scharlau), 1 mol HCl per mol of Ti+Nb, and ultrapure water, 50 mol water per mol of Ti+Nb, were added to the mixture, vigorously stirring at room temperature for 1 h. Then, the gellification of the sol was produced by the addition of aqueous solution of 1.0 M $(NH_4)_2CO_3$ [31,32]. The final product was filtered, rinsed and dried at 60 ºC for 10 h and afterwards, it was calcined at 350 °C in air atmosphere for 2.5 h [55].

A modified hydrothermal technique based on those previously reported in the literature for TNTs [23,55-57] and Nb-doped materials [58,59] was applied for the synthesis of the TNTs and Nb-doped TNTs. The doping concentration of Nb was 3, 6, and 10 at %, being respectively denoted as 3Nb-TNTs, 6Nb-TNTs, and 10Nb-TNTs. The amount of 1 g of

the synthesized TiO_2 or Nb-doped TiO_2 was dispersed in 100 mL of 10.0 M NaOH and placed in a Teflon® autoclave. The mixture was sonicated for 2 h and then, it was heated for 72 h at 130 °C [60]. The (Nb-doped) sodium titanates ($Na_2Ti_xO_{2x+1}$) thus obtained were protonated with 0.1 M HCl [61,62], which were rinsed with ultrapure water and dried at 60 ºC for 10 h. Finally, the calcination of the (Nb-doped) protonated titanates ($H_2Ti_xO_{2x+1}$) at 350 °C for 2.5 h allowed obtaining the TNTs and Nb-doped TNTs.

Pt nanoparticles were dispersed on the indicated supporting materials by means of the conventional electroless deposition method, using $NaBH_4$ as reducing agent and sodium citrate as stabilizing agent [63]. The appropriate amount of support was dispersed in ultrapure water, followed by the addition of $H_2PtCl_6 \cdot 6H_2O$ (99.9 % metal basis, Alfa Aesar) to achieve a loading of 20 wt. % Pt in the final solid, and sodium citrate (Sigma Aldrich). The suspension was neutralized to pH 7.0 and stirred for 10 h at 50 ºC before adding the $NaBH_4$ (Sigma Aldrich). Finally, the suspension was filtered, rinsed with ultrapure water and dried at 60 ºC until constant weight. The resulting catalysts were then Pt/*n*Nb-TiO_2 and Pt/*n*Nb-TNT, *n* indicating the Nb content (with values of 0, 3, 6 and 10 at %). It has been reported that the Nb-doped TiO_2 catalysts have conductivities about 10^{-3} S cm^{-1} and that they increase with Nb doping [29], which is small compared to those reported for Vulcan carbon XC72 and XC72R of 4.5 [64] and 2.8 S cm^{-1} [65], respectively. However, the Pt deposition can significantly change the conductivity of the sample, as previously shown when the conductive IrO_2 was deposited on Nb-doped TiO_2 [29]. In this case, the conductivity of the latter was increased in this form by one or two orders of magnitude. Commercial 20 wt. % Pt on Vulcan XC72 catalyst (Pt/C) from Premetek was taken as a reference for comparison purposes.

2.2. Physicochemical characterization of the supports and catalysts

The SEM images of the titania supports were taken using a JSM5910-LV JEOL microscope. The Nb:Ti atomic ratios of the supports and the mass ratio of the metal to the support in the electrocatalysts was analyzed by the energy dispersive X-ray (EDX) technique, using an INCA-300 energy analyzer coupled to the scanning electron microscope.

The catalysts were examined by TEM, using a JEOL JEM-1400PLUS microscope, equipped with a GATAN US1000 CCD camera (2k×2k) and operating at 120 kV. Prior to the observation, the specimens were dispersed and sonicated for 10 min in ethanol, and then deposited onto a carbon-coated copper grid.

The textural properties of the supports were determined by N_2 adsorption/desorption isotherms at 77 K, using a Micromeritics ASAP 2020 instrumentation, after outgassing for 10 hours at 150 °C under vacuum (10^{-5} torr). The specific surface area (S_{BET}) was determined using the Brunauer-Emmet-Teller (BET) equation and taking 0.162 nm^2 as the cross-sectional area of the N_2 molecule. The pore volumes and pore size distributions were obtained from the desorption branches of isotherms by means of the Barret-Joyner-Halenda (BJH) model.

The XRD patterns were obtained by a Bruker D8 Advance diffractometer operating with Cu K_α radiation (λ=1.5406 Å) and a 2θ scan from 5 to 80° (at 0.01° min^{-1}). The diffraction peaks were assigned according to the International Centre for Diffraction Data (ICDD) cards in PDF-2 database. The XRD data were used to determine the lattice parameter from the interplanar distances, and the average crystallite size by using Scherrer equation [66].

The XPS experiments were performed in a SPECS Sage HR 100 spectrometer with a non-monochromatic X ray source of Magnesium with a K_α line of 1253.6 eV energy and

250 W. The selected resolution for the high-resolution spectra was 15 eV of Pass Energy and 0.15 eV $step^{-1}$. Measurements were made in an ultra-high vacuum (UHV) chamber at a pressure around 8×10^{-8} mbar. The samples were placed perpendicular to the analyzer axis and the internal calibration was performed using the 1s line of adventitious carbon at 284.6 eV. Asymmetric and Gaussian Lorentzian functions were used for the band deconvolution (after a Shirley background correction), constraining the full width at half maximum (FWHM) of all the peaks and setting free the peak positions and areas.

2.3. Electrode preparation and electrochemical characterization

An amount of 10 mg of the catalyst was dispersed in 0.50 mL mixture of isopropanol and ultrapure water (1:1 by volume), and sonicated for 30 min. The required amount of this suspension was placed by means of a micropipette onto the surface of a glassy carbon (GC) disk (0.0707 cm^2 in section) to achieve a Pt loading of 14 $\mu g_{Pt} cm^{-2}$ and dried under a slow nitrogen flow (Air Liquide, purity ≥ 99.995 %). It was then covered with 5µl of a 0.05 % Nafion® solution diluted in ethanol and dried again under nitrogen. Before each analysis, the GC disk was polished to a mirror finish using alumina powder suspensions (0.3 µm and 0.05 µm, Buehler), followed by sonication in water.

The electrochemical measurements were conducted with a potentiostat PARSTAT 2273 (Ametek, Inc.) controlled by the PowerSuite 2.58 software in a thermostatic three-electrode glass cell at 25.0 ± 0.1 ºC. The cell was placed inside a Faraday cage, and the experiments were carried out under dark conditions (to avoid any possible photoelectrocatalytic effect coming from the studied materials). The working electrode was the catalyst-covered GC one and the reference electrode was the mercurous sulfate electrode (MSE) $Hg|Hg_2SO_4|K_2SO_{4(sat)}$ (Radiometer Analytical). However, all the potentials reported in this work are expressed *vs.* the reversible hydrogen electrode (RHE). The auxiliary electrode was a Pt wire and the electrolyte was an aqueous solution

0.50 mol dm^{-3} H_2SO_4 (prepared from Merck Suprapure®), deaerated by N_2 bubbling through the solution for 20 min.

For the electrochemical experiments, the electrode was immersed into the N_2-purged electrolyte, and it was cycled in the potential window 0.050–1.200 V at a scan rate of 100 mV s^{-1} until reproducible cyclic voltammograms were obtained. The Pt ECSA was estimated from the net charge for hydrogen adsorption/desorption profiles in the cyclic voltammograms recorded at scan rate 20 mV s^{-1} under N_2 inert atmosphere, assuming that a charge of 210 μC cm^{-2} was needed to produce a monolayer of adsorbed H on polycrystalline Pt [67].

The HER was studied by LSV without stirring in a cathodic sweep in the range from 0.100 to -0.100 V at a scan rate of 1 mV s^{-1} and with ohmic-drop correction. The *IR*-drop in solution was measured using electrochemical impedance spectroscopy. The impedance spectra were obtained at the open circuit potential, in the frequency range from 100 kHz to 0.1 Hz, superposing an *ac* amplitude of 5 mV. All these *j-E* curves were corrected by the uncompensated resistance and repeated three times for each catalyst to test their reproducibility.

3. Results and discussion

3.1. Physicochemical characterization of the supports based on TiO_2 and TNTs

The different morphology of the TiO_2 and TNTs supports are exemplified in Figs. 1 and 2. Fig. 1a and b shows the SEM images of TiO_2 and TNTs with 3 at % Nb doping, respectively, where the different size and morphology of the constituent particles are apparent. A prismatic shape typical of TiO_2 is shown in Fig. 1a, with evident porosity, whereas the morphology of the TNTs is completely different, with randomly oriented thin

nanotubes looking like a cobweb, in which greater porosity and specific surface area are expected.

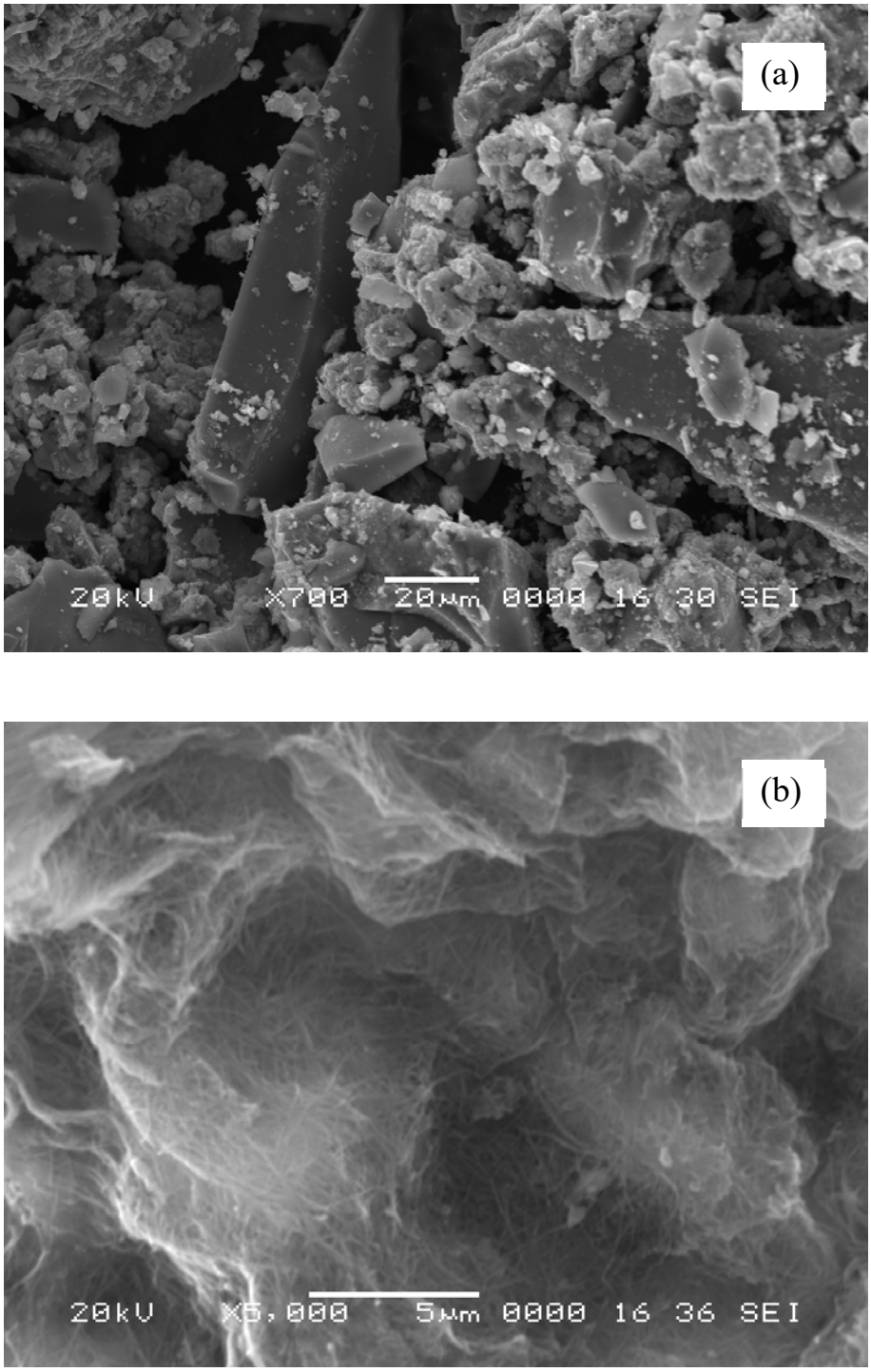

Fig. 1 – SEM images of different supports: (a) 3 Nb-TiO_2 and (b) 3Nb-TNTs.

Details at different magnifications of 3Nb-TNTs are shown in the TEM pictures of Fig. 2a and b. The TEM image of Fig. 2b shows the Nb-doped nanotubes, which were about 10 nm in the outer diameter and in the range 100-200 nm in length. A high-resolution image of the same support is given in Fig. 2c, where the end of a nanotube together with the corresponding selected area electron diffraction (SAED) are shown. The string pattern of the SAED is the expected one for a tube-shaped crystal [56] and it is in agreement with previous work showing that the nanostructures produced by hydrothermal reaction depend on different process parameters. Thus, nanotubes were obtained from TiO_2 crystals, whereas nanofibers with interlinked structure were formed from amorphous TiO_2 [68], the SAEDs of the latter presenting diffuse rings of amorphous phases.

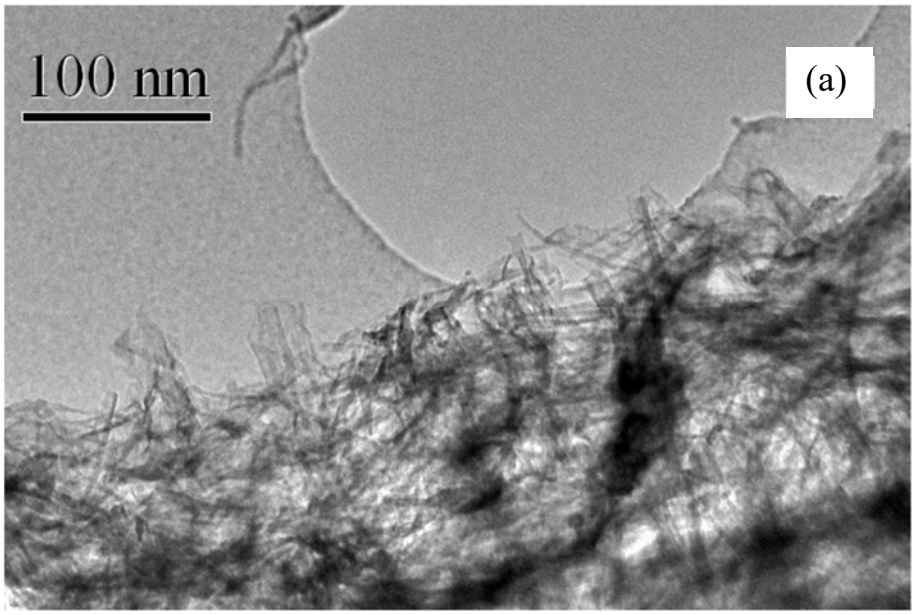

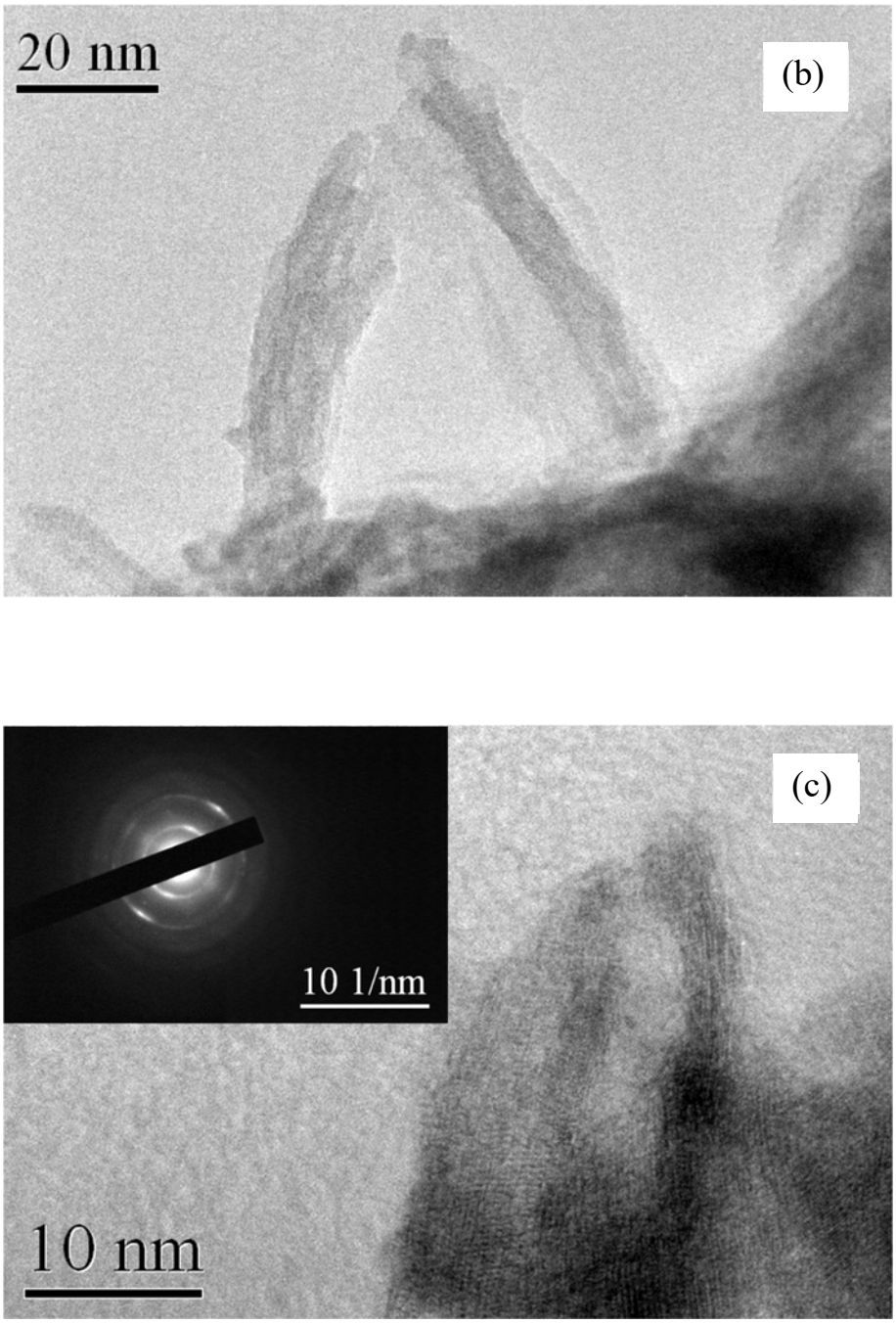

Fig. 2 – TEM pictures of 3Nb-TNTs at different magnifications: (a) general view, (b) detail of the nanotubes and (c) a high-resolution image of a nanotube with the corresponding SAED in the inset.

The textural properties of the supports studied are listed in Table 1. The specific surface areas, S_{BET}, for TiO_2 and Nb-doped TiO_2 are in the range 80-100 m^2 g^{-1}. As shown in this table, the surface area increased with the Nb content, although the corresponding pore diameter and volume decreased. The same trend in S_{BET} and pore diameter can be observed for TNTs doped with Nb, the specific surface areas rising from 145 to 303 m^2 g^{-1}, values corresponding to the undoped and to a Nb doping of 10 at %, respectively. In this case, however, the pore volume increased with the Nb content. It is worth to note that the pore volumes and diameters, together with the surface areas were about 2-3 times greater for the TNTs. These changes in the textural properties appeared to be due to the different size of the titania nano-building blocks generated during the synthesis procedure, which were packed in a different form during calcination [29,39].

Surface areas of 68 and 143 m^2 g^{-1} were previously reported in the literature for mesoporous titania, without Nb doping and with 5 at % Nb, respectively, with no further significant change when Nb doping was increased to 20 at % [29]. The surface areas reached with the Nb-doped TNTs of this work were greater than previous values reported in the literature for $Nb_{0.05}Ti_{0.95}O_2$ powders (83 m^2 g^{-1}) [38] and mesoporous $Nb_{0.1}Ti_{0.9}O_2$ (147 m^2 g^{-1}) [29]. The surface areas of the Nb-doped TNTs obtained in this work were also greater than that reported for commercial Vulcan XC72 (Cabot Corp.), one of the most used carbon black as catalyst support, with a value of about 250 m^2g^{-1} [11,12,65]. Therefore, the Nb-doped TNTs appeared to be suitable for application as catalyst supports in porous diffusion electrodes. Compared to these values, the surface areas of TiO_2 were somewhat smaller and then, TNTs seem to be better candidates as catalyst supports.

The X-ray diffractograms of the supports based on TiO_2 and TNTs with different Nb contents are depicted in Fig. 3a and b, respectively. The typical peaks of the anatase phase of titania have been clearly identified for both supports. It is also shown in these figures

that when the amount of Nb increased, the anatase peaks became wider, thus suggesting smaller anatase crystallite size with Nb doping. The mean crystallite size was estimated from Scherrer's equation and the corresponding results are also listed in Table 1. It is shown that the crystallite sizes for Nb-doped TiO_2 (in the range 6.4-7.3 nm) were smaller than that for undoped TiO_2 (8.7 nm). Similar results were found for the TNTs, the values for the Nb-doped TNTs being smaller (in the range 6.5-7.8 nm) than for the undoped ones (8.8 nm). This agrees with the previously observed grain growth inhibition by the Nb dopant in titania nanopowders [32] and in $Pb(ZrTi)Nb_xO_3$ (x = 0.02–0.06) ceramics [69]. The Nb effect can then be explained in the same form. The vacancies created by Nb doping are supposed to be bound to Nb. As the grain growth involves the lattice diffusion of vacancies from pores to grain boundaries, the doping Nb ions can diminish the mobility of the vacancies and concentrate near the grain boundaries, thus resulting in smaller grain size. Note, however, that when the Nb content increased, the crystallite size also increased, although remaining under the crystallite size of the undoped titania. This may be related to the increase in the number of vacancies created with rising the Nb content, because such vacancies are needed for the grain growth.

Table 1 – Textural properties from BET analysis of N_2 adsorption, and crystallite size and lattice parameters from XRD, of the different supports studied.

Support	Nb content[a] / at %	Pore volume / $cm^3\ g^{-1}$	Pore diameter / nm	S_{BET} / $m^2\ g^{-1}$	Crystallite size / nm	Lattice parameter / Å
TiO_2	0.0	0.202	7.08	80	8.7	4.9782
3Nb-TiO_2	3.3	0.178	6.05	87	6.4	4.9860
6Nb-TiO_2	6.2	0.165	4.87	93	6.5	4.9865
10Nb-TiO_2	10.8	0.126	3.77	100	7.3	4.9978
TNT	0.0	0.581	13.4	145	8.8	4.9865
3Nb-TNT	3.1	0.769	9.33	260	6.5	5.0007
6Nb-TNT	6.1	0.817	9.25	278	6.9	5.0049
10Nb-TNT	11.1	0.861	9.13	303	7.8	5.0544

[a] Mean standard deviation of 0.3 at %

Fig. 3a and b also shows a slight shift of the peaks toward lower angles when titania is doped with Nb, thus predicting a lattice expansion with the Nb introduction in the titania lattice. Bragg's law allowed determining these lattice parameters, which are also given in Table 1. These values clearly confirm the lattice expansion with Nb doping, the lattice parameter increasing with the Nb content due to the higher size of Nb(V) with respect to Ti(IV). These results are also consistent with previous ones reported in the literature for rutile 10Nb-TiO_2, with a greater lattice parameter than rutile TiO_2 [70].

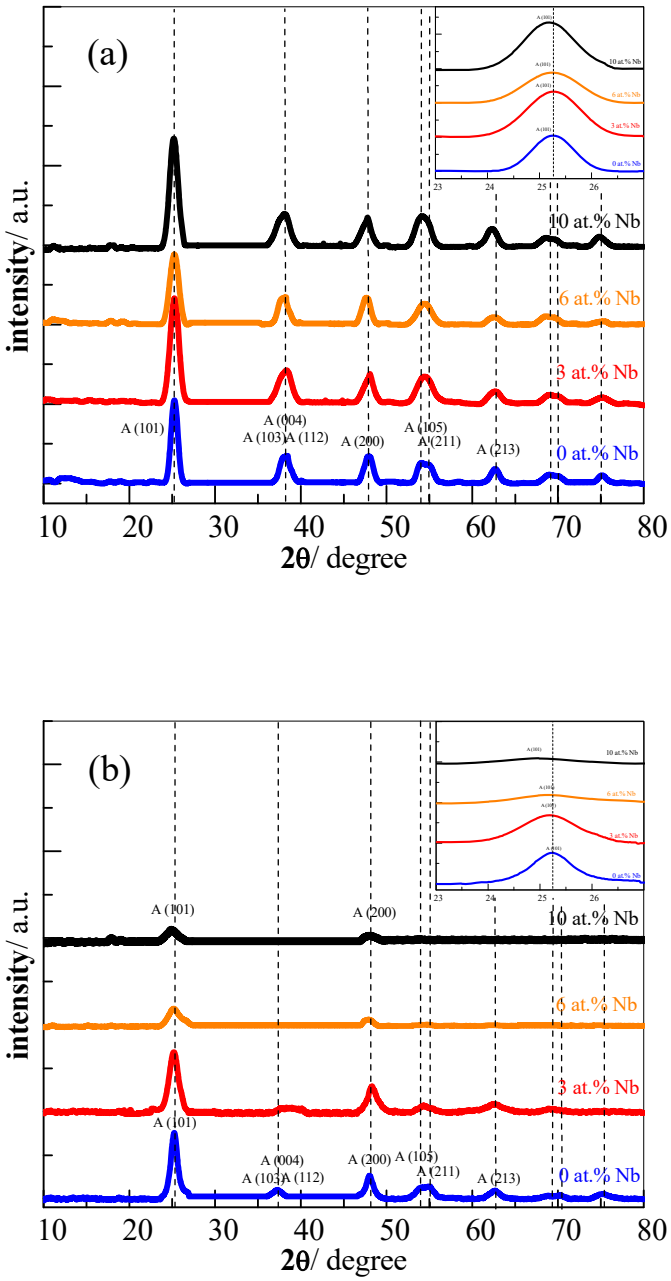

Fig. 3 – X-ray diffractograms of the supports with different Nb content: (a) TiO_2 and (b) TNTs. In parentheses, planes corresponding to characteristic diffraction signals of anatase, A. The inset is a magnification of peak A(101) to show its displacement towards smaller angles with Nb doping.

3.2. Physicochemical characterization of Pt electrocatalysts

Fig. 4 depicts selected TEM images of the 20 wt % Pt/3Nb-TNT catalyst. Fig. 4a shows that the Pt nanoparticles were homogeneously dispersed over the TNTs. Such a dispersion suggests a suitable contact between the catalyst and the support and allows providing a good electronic conductivity of the supported catalyst [71,72]. The compositional results obtained from the EDX analyses performed by SEM are given in Table 2.

Table 2 – Structural and electrochemical characteristics of Pt supported to 20 wt % on the different Nb-doped TiO_2 and TNTs.

Electrocatalyst	**Pt content[a] / wt %**	**Crystallite size / nm**	**Lattice parameter / Å**	**ECSA / m^2 g^{-1}**
Pt/TiO_2	20.7	4.9	3.92	12
Pt/3Nb-TiO_2	18.8	4.1	3.92	14
Pt/6Nb-TiO_2	19.2	4.6	3.93	11
Pt/10Nb-TiO_2	18.1	5.2	3.92	12
Pt/TNT	19.6	4.4	3.93	14
Pt/3Nb-TNT	20.7	3.9	3.92	11
Pt/6Nb-TNT	18.8	4.9	3.92	13
Pt/10Nb-TNT	17.6	4.5	3.93	11

[a] Mean standard deviation of 0.9 wt %

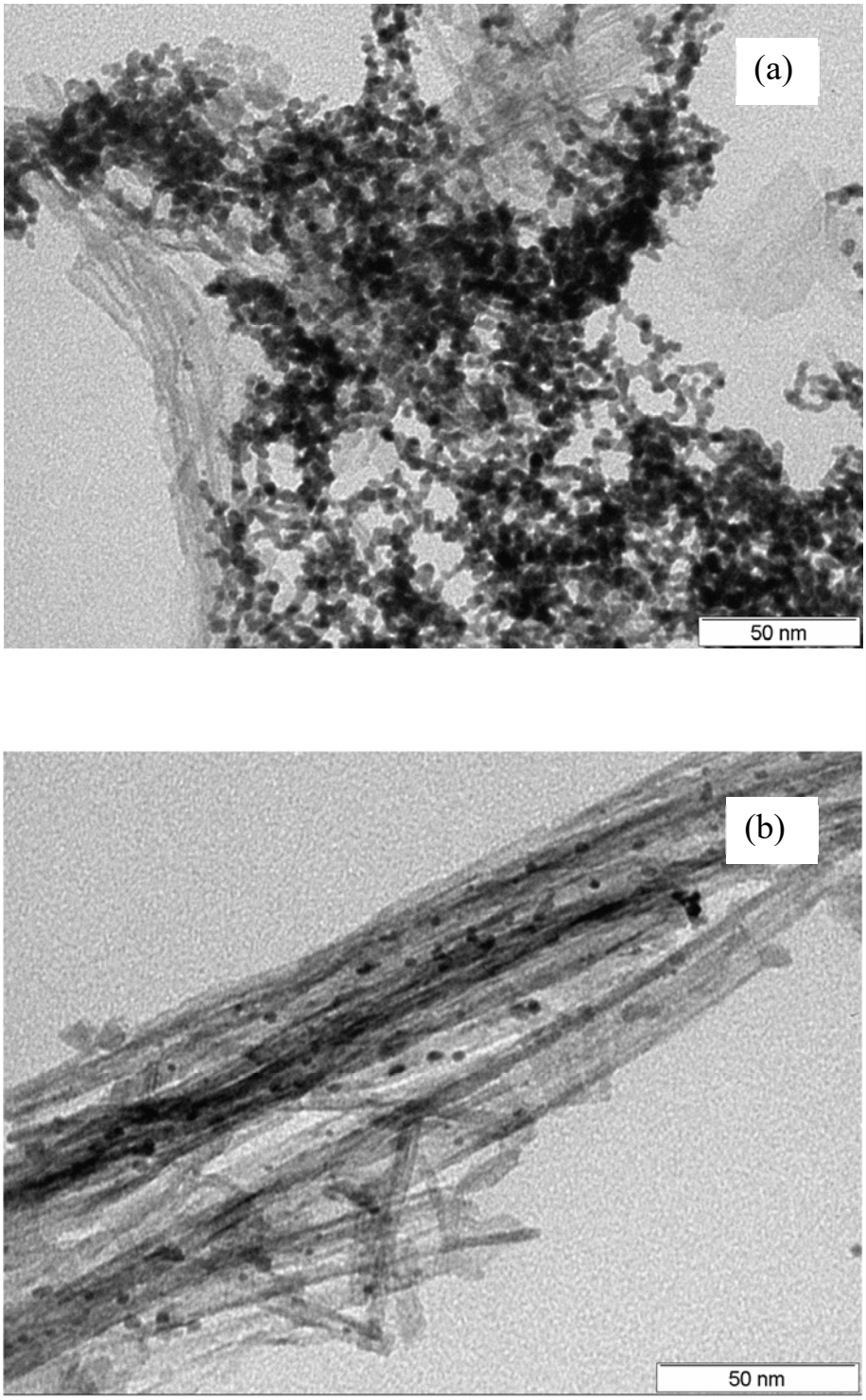

Fig. 4 – TEM pictures of 20 wt % Pt/3Nb-TNT at different magnifications: (a) general view and (b) detail of the Pt dispersion on the nanotubes.

The diffractograms corresponding to Pt supported on TiO_2 and on TNTs for different Nb contents are depicted in Figs. 5a and b, respectively. Typical peaks for (111), (200) and (220) planes, characteristic of the face-centered cubic (*fcc*) lattice structure of platinum, which appear at 2θ values of 39.7, 46.2 and 67.6, respectively, are indicated. In all cases, it is shown that Pt peaks are superimposed to the anatase ones shown in Figs. 3a and b. From Scherrer equation and Bragg's law, the corresponding crystallite sizes and lattice parameters were obtained (see Table 2). The lattice parameters were always found to be close to a = 3.922 Å, confirming that the nanoparticles consisted of pure Pt. The crystallite sizes, estimated from the (111) Pt peak, are also listed in Table 2. Values in the range 4.1-5.2 Å were obtained for the Pt nanoparticles supported on TiO_2, whereas they were in the range 3.9-4.9 Å for TNTs. This difference is small, but it seems that there is some dependence on the support. With 3 at % of Nb doping, the Pt crystallite size is smaller than that on the non-doped titania (TiO_2 and TNTs). However, it increases with further additional Nb doping. The smaller crystallite size of Pt for 3Nb-TiO_2 and 3Nb-TNT can be explained by the nucleation at more sites of the later supports with respect to TiO_2 and TNTs due to an increase in the surface area (Table 1). The increase in the crystallite size of Pt with further Nb doping does not match with the corresponding increase in the BET surface area. This appears to be related to the pore diameter, since according to Table 1, it decreases when the Nb content increases and then, the surface area increase is probably less effective in providing more nucleation sites. This is more marked in the case of the TiO_2 supports, which have smaller pore diameters than those of TNTs and consequently, the corresponding Pt crystallite sizes on the former are somewhat greater.

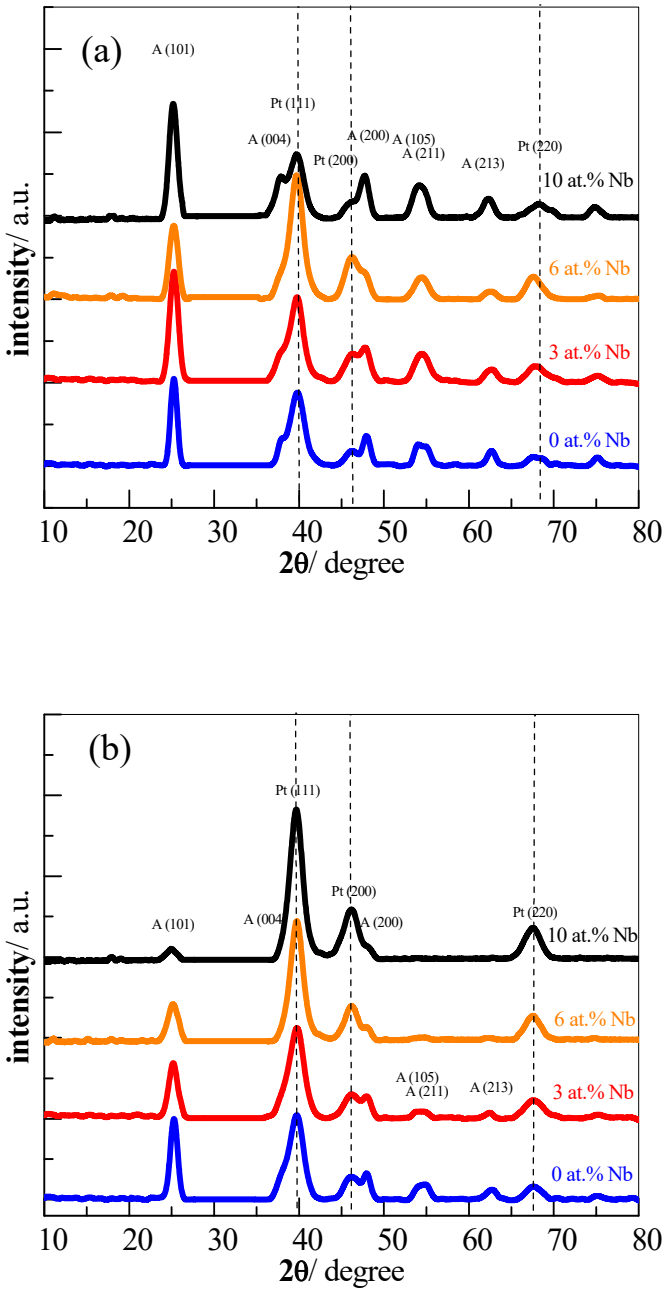

Fig. 5 – X-ray diffractograms of Pt supported to 20 wt % on (a) TiO_2 and (b) TNTs, with the indicated Nb contents. In parentheses, planes corresponding to characteristic diffraction signals of anatase, A, and *fcc* Pt.

Fig. 6a and b shows the Pt 4f XPS spectra of 20 wt % Pt/C and of 20 wt % Pt/3Nb-TNT, respectively. As shown in Fig. 6a, the main Pt $4f_{7/2}$ and Pt $4f_{5/2}$ peaks of 20 wt % Pt/C are located at about 71.43 and 74.73 eV, and can be mainly assigned to Pt(0) [73]. Similar results have been obtained for 20 wt % Pt/3Nb-TNT, with the respective Pt $4f_{7/2}$ and Pt $4f_{5/2}$ peaks located at about 71.31 and 74.61 eV, which can also be assigned to Pt(0) [73]. There is a shift of the Pt 4f signal of about 0.12 eV for Pt/3Nb-TNT to lower binding energies in comparison to the Pt/C reference catalyst. This difference suggests a local increase of the electron density on Pt in the former with respect to the later, thus suggesting a SMSI between Pt and the support in Pt/3Nb-TNT, comparable to that previously claimed for Pt-TiO_2 [24-27], which favored the kinetics of the oxygen reduction reaction, due to such a positive effect of the substrate.

With regard to the peaks deconvolution, also shown in Figs. 6a and b, the Pt(0) and Pt(IV) signals have been considered. Note that the Pt(0) component was fitted to an asymmetric shape, which is characteristic of conductive materials. The deconvolutions depicted in Figs. 6a and b clearly show that the main contributions are due to Pt(0). The Pt(IV) ones are minor and the Pt $4f_{7/2}$ peaks of 20 wt % Pt/3Nb-TNT and 20 wt % Pt/C are located at about 76.57 and 77.00 eV, respectively, the bonding energy shift being also in agreement with the different chemical nature of both supports.

The binding energy regions of Ti, O and Nb for 20 wt % Pt/3Nb-TNT are depicted in Figs. 6c, d and e, respectively. In Fig. 6c, the main Ti $2p_{3/2}$ peak is located at about 458.5 eV, which corresponds to Ti(IV), bond with oxygen in TiO_2 [29,39]. The characteristic shake-up peaks of TiO_2 are also observed and shown in the figure. We tried the deconvolution of the Ti peaks considering the possibility of Ti(III), with binding energies of 457.8 and 463.2 eV [29], but no convincing results were obtained and therefore, if present, it would be in a very small amount. It is also worth to mention that in a previous

work of the authors using the same supports with Ir-based catalysts [39], the smaller binding energy of Ti(IV) in TNTs was 458.8, but changed to 458.4 eV in 3Nb-TNTs, value which is close to that found in this paper. This means that the electronic state of Ti was slightly modified from pure Ti(IV) when going from TNTs to 3Nb-TNTs.

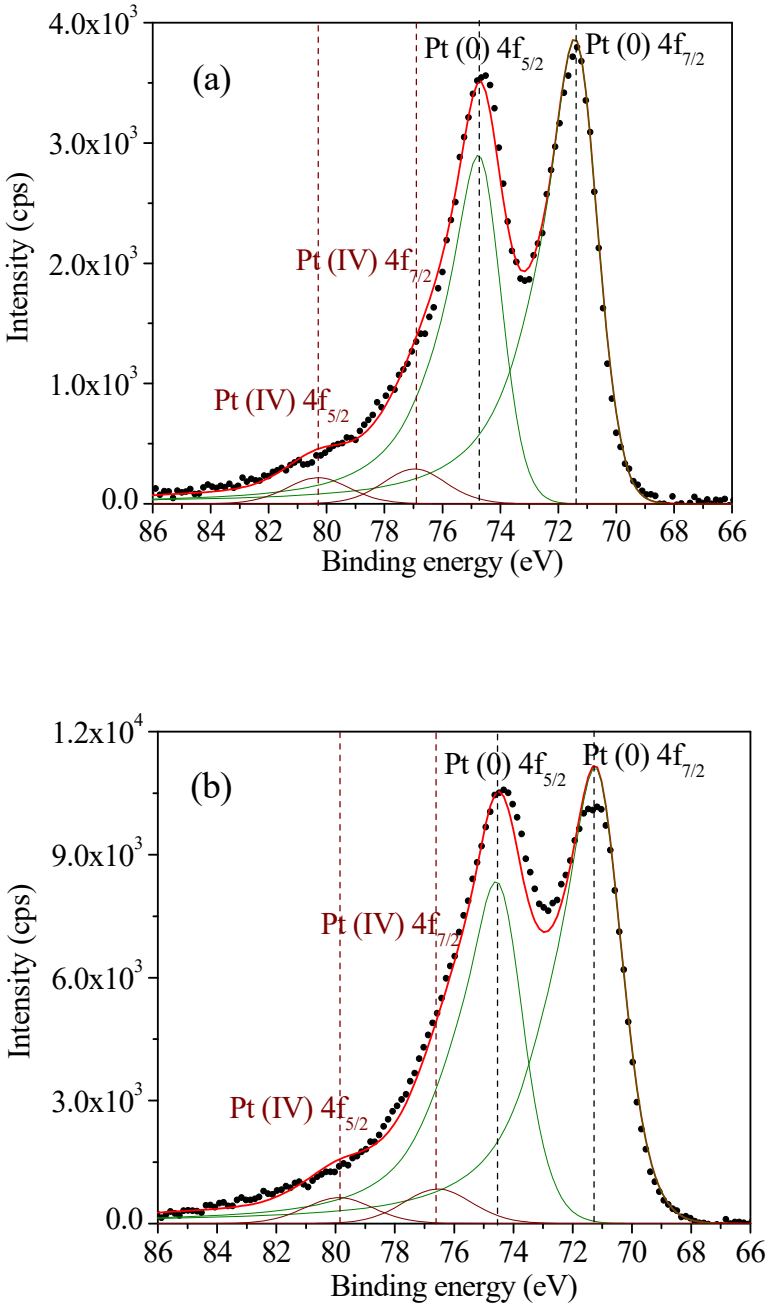

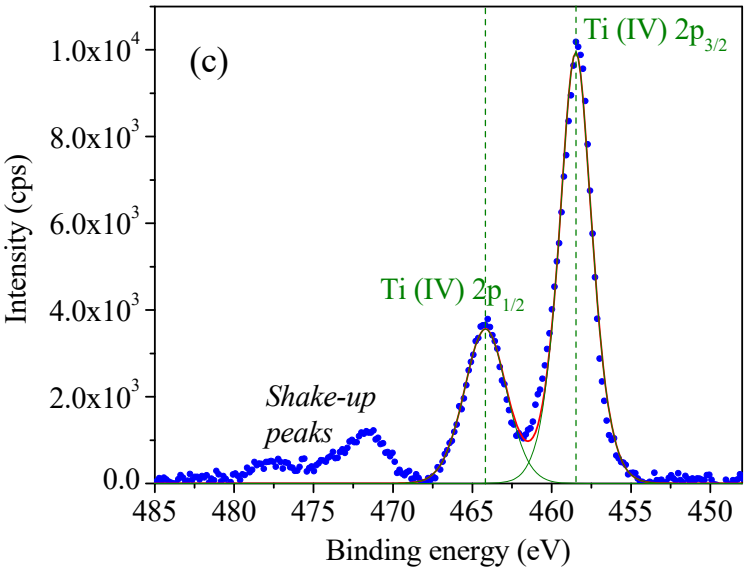
(c)
Ti (IV) 2p3/2
Ti (IV) 2p1/2
Shake-up
peaks
Intensity (cps)
Binding energy (eV)
1.0x10^4
8.0x10^3
6.0x10^3
4.0x10^3
2.0x10^3
0.0
485
480
475
470
465
460
455
450

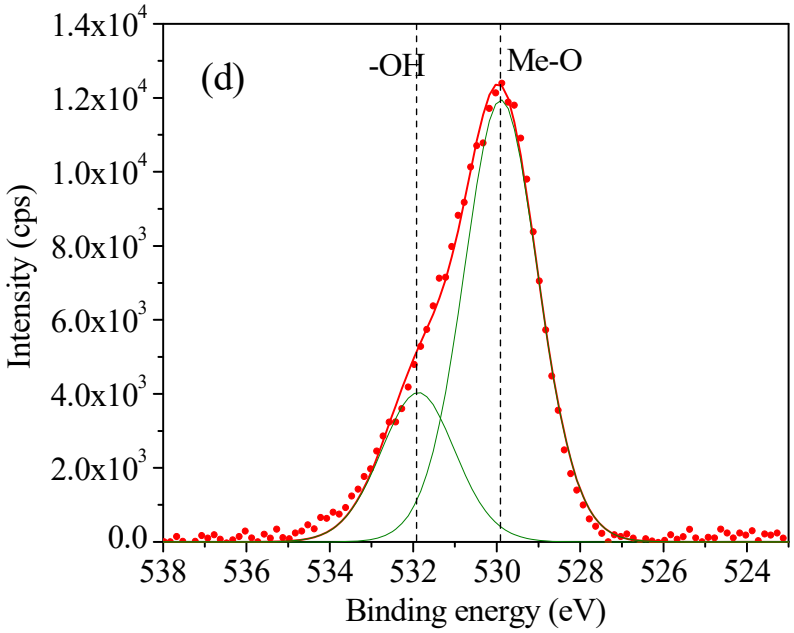
(d)
-OH
Me-O
Intensity (cps)
Binding energy (eV)
1.4x10^4
1.2x10^4
1.0x10^4
8.0x10^3
6.0x10^3
4.0x10^3
2.0x10^3
0.0
538
536
534
532
530
528
526
524

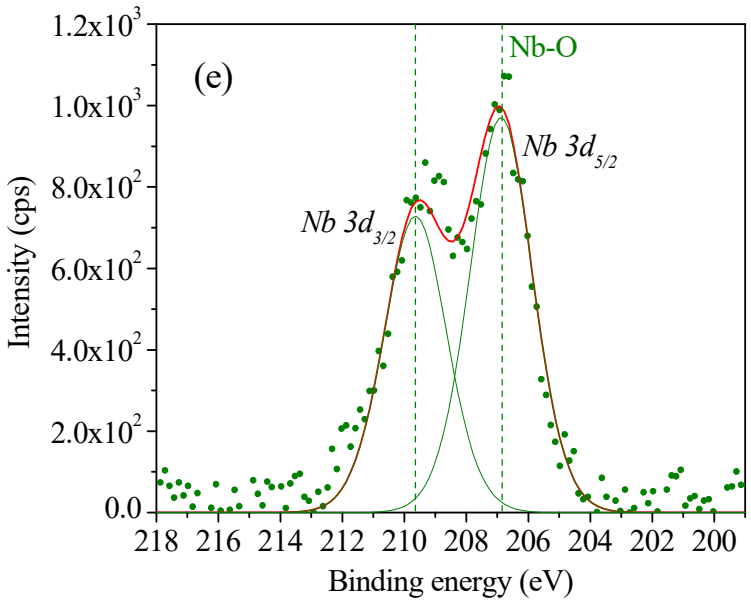

Fig. 6 – High-resolution XPS spectra in the different binding energy regions of (a) Pt 4f for 20 wt. % Pt/C and (b) Pt 4f, (c) Ti 2p, (d) O 1s and (e) Nb 3d for 20 wt % Pt/3 Nb-TNT.

Fitting of the O1s binding energy profile revealed the presence of two components (see Fig. 6d), the main one at around 529.9 eV, which could be attributed to oxygen from the Nb-TNTs. This one appears at a somewhat smaller BE than that of 530.6 eV reported for oxygen from TiO_2 [27], but this could be due to the different support composition. On the other hand, the smaller BE peak at around 531.9 eV could be due to surface -OH groups, oxygen species on carbon and carbonate species, which can be expected on the surface of this kind of supports. The same value of 531.9 eV was assigned for all present oxygen-containing species on carbon and Pt, including Pt oxides on Pt/C [27]. In our case, the presence of Pt(IV) oxide is not probable because the Pt(II) signal is missing and the small Pt(IV) signal appears at 76.5-77.0 eV instead of at 74.2 eV [74], thus indicating that the former is probably related to the cation bonding to very electronegative species such as chloride.

On the other hand, Fig. 6e shows that the main Nb $3d_{5/2}$ binding energy peak is located at around 206.8 eV, which can be attributed to the Nb-O bonds in NbO_2 [29,39,73]. This value is somewhat higher than that one of 206.0 eV reported previously in the literature for Nb(IV) [29]. For this reason, we also tried the deconvolution of the Nb peaks considering the Nb(V) species, with binding energies of 207.5 and 210.2 eV [29], but this was not feasible. However, it is interesting to note that the Nb(IV) peaks in Fig. 6e slightly tended to Nb(V) (i.e. to higher BEs) whereas the Ti(IV) peaks of Fig. 6c slightly tended to Ti(III) (i.e. to lower BEs). This suggests some electronic modification in both, Ti and Nb in 3Nb-TNTs, which can be explained considering that this low valence state of Nb in the oxide can generate an electron donor level in the forbidden region of the titania bandgap. The shift of the O1s peak to a smaller BE of Fig. 6d when compared to that from TiO_2 [27] is also in agreement with the electron donor characteristics of Nb. This would lead to free electrons in the conduction band of titania, which would increase the conductivity of the support [75].

3.3. Electrochemical characterization of the Pt electrocatalysts

Control CV experiments in deaerated 0.50 mol dm^{-3} H_2SO_4 were first performed to analyze the *j–E* profile of the Pt nanoparticles deposited on the different supports. Fig. 7a and b shows the cyclic voltammograms corresponding to Pt supported on TiO_2 and TNTs, respectively, after normalizing with respect to the ECSAs (see Table 2). These were determined from the ratio between the charge associated to the hydrogen adsorption/desorption peaks of the cyclic voltammograms and the Pt load ($\mu C\ \mu g_{Pt}^{-1}$), divided by a charge of 210 $\mu C\ cm^{-2}$ for a monolayer formation of adsorbed hydrogen on polycrystalline Pt [76]. The real current densities plotted in Fig. 7a and b were then obtained by dividing the specific current densities ($mA\ \mu g_{Pt}^{-1}$) by the corresponding ECSAs.

The values of the ECSAs varied in the range 11–14 $m^2\ g_{Pt}^{-1}$ (see Table 2), that is without significant differences for the two types of supports used. The results listed in Table 2 indicate that comparable nanoparticle size, dispersion and aggregation were obtained by means of the electroless deposition of Pt, performed under the same conditions, on the different supports studied. Note that these values were smaller than that determined for commercial Pt/C, which was of 43 $m^2\ g_{Pt}^{-1}$, due to its smaller nanoparticle size. The *j*–*E* profile normalized by the ECSA corresponding to Pt/C is depicted in curve *i* of Fig. 7c. It is shown in Fig. 7c that the normalized *j*–*E* profiles of Pt supported on TiO_2 (curve *j*) and TNTs (curve *k*) match very well with that of commercial Pt/C.

Fig. 7a and b shows the typical features of polycrystalline Pt for all the supported catalysts studied [77], thus indicating good Pt-support interaction. The peaks corresponding to hydrogen adsorption/desorption, in the potential range 0.03–0.30 V, are well resolved. The Pt oxidation started at about 0.75 V and the cathodic peak potential at about the same potential corresponded to the Pt oxide reduction.

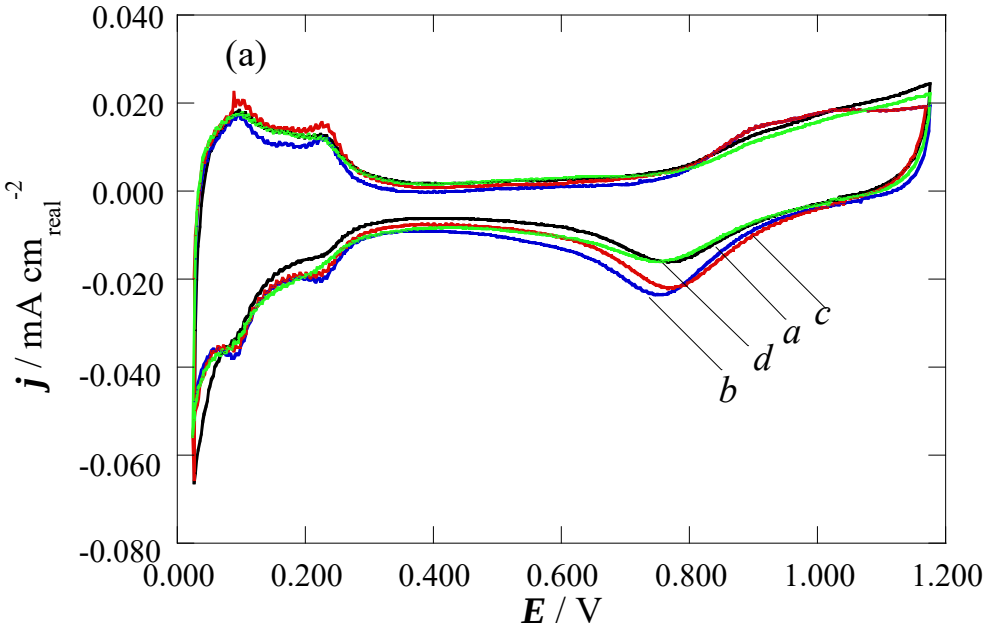

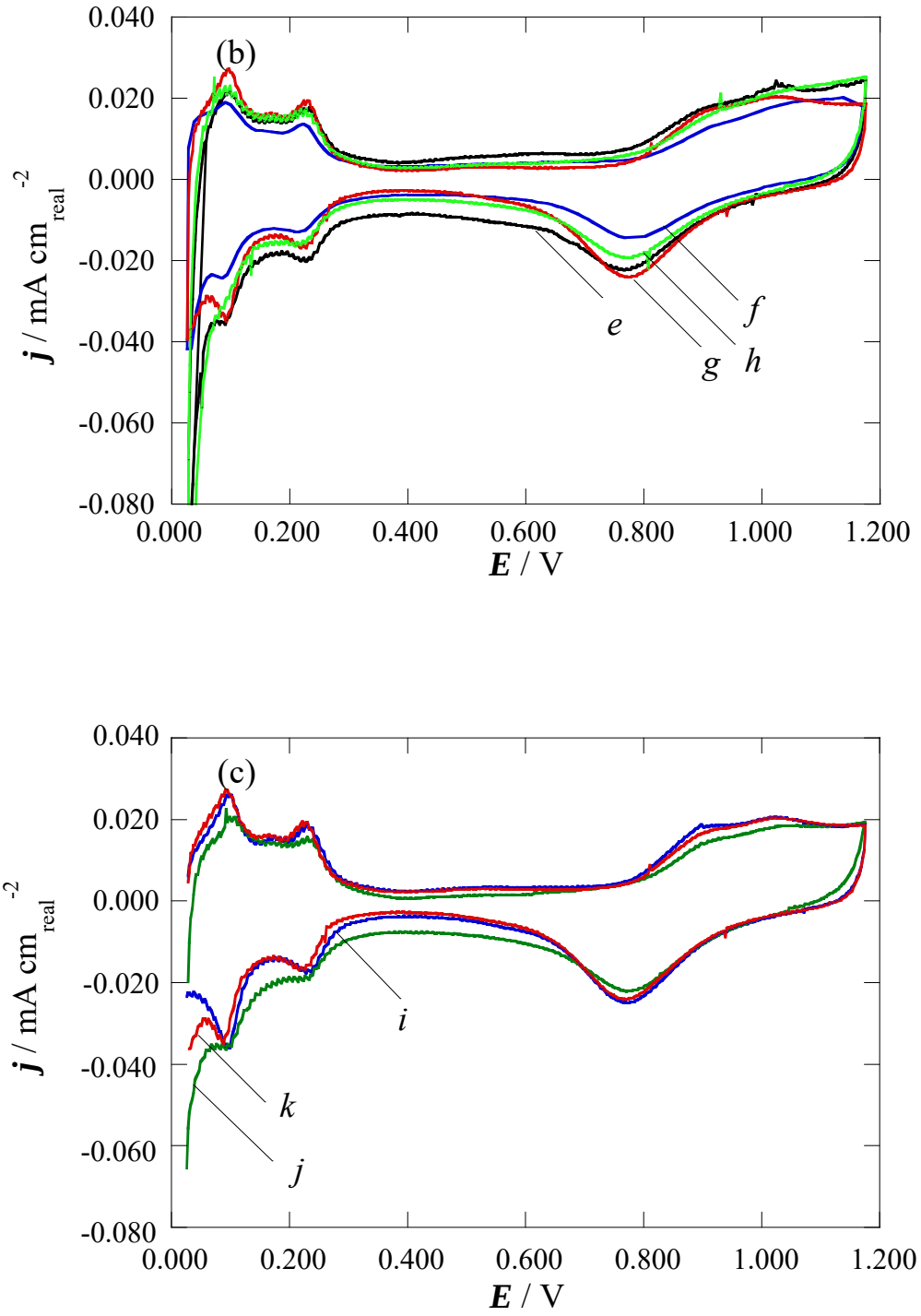

Fig. 7 – Cyclic voltammograms in deaerated 0.50 mol dm^{-3} H_2SO_4 at 20 mV s^{-1} for 20 wt % Pt on (a) TiO_2-based and (b) TNTs-based supports. Figure (c) corresponds to commercial Pt/C compared to Pt supported on TiO_2 and TNTs. The different *j–E* curves correspond to (*a*) Pt/TiO_2, (*b*) Pt/3Nb-TiO_2, (*c*) Pt/6Nb-TiO_2, (*d*) Pt/10Nb-TiO_2, (*e*) Pt/TNT, (*f*) Pt/3Nb-TNT, (*g*) Pt/6Nb-TNT, (*h*) Pt/10Nb-TNT, (*i*) commercial Pt/C, (*j*) Pt/6Nb- TiO_2 and (*k*) Pt/6Nb-TNT. *IR*-drop corrected. The current densities have been referred to the corresponding ECSAs.

Fig. 8a and b depicts the linear sweep voltammograms corresponding to the HER in deaerated 0.50 mol dm^{-3} H_2SO_4 at 1 mV s^{-1} on Pt deposited on the TiO_2-based and the TNTs-based supports, respectively. All the curves shown in Fig. 8a and b start with an exponential current density increase with potential. However, for current densities above 10 mA cm^{-2}, the hydrogen bubbles evolved from the working electrode significantly affected the shape of *j–E* curves. Note that these curves move in a potential range of about 10 and 20 mV for the TiO_2 (Fig. 8a) and TNTs supports (Fig. 8b), respectively. As long as the experimental error was better than 5 mV, the different *j–E* plots denoted different catalyst activity, despite the Pt nanoparticles have about the same size and ECSA, on all the supports studied (see Table 2). This different performance could then be explained by a different Pt-support interaction, which depended on the support. Nb doping of TiO_2 and TNTs generally led to better electrocatalyst activity, what can be explained by the local increase of the electron density on Pt due to the SMSI discussed above, favored by the Nb doping, in particular for the TNTs. It is apparent from the *j–E* plots of Fig. 8a and b that the Pt catalysts supported on TiO_2 and TNTs doped with 3 and 6 at % Nb showed the highest catalytic activity, because the current densities at a given potential were greater than for the other supports. Some reduction in the catalyst activity is observed when Nb doping increases to 10 at %. This is probably related to the pore diameter decrease when increasing the Nb doping, despite that the specific surface area increased, feature that can limit the accessibility to the nanoparticles.

From a quantitative point of view, it is useful to provide some characteristic parameters used to evaluate the HER performance of the different catalysts, such as the potential required to achieve a current density relevant for the electrolyzer design [54,78,79]. Thus, the potential required to achieve a j = -0.010 A cm^{-2} (E_{10}) were measured for each catalyst studied in this paper and the corresponding results have been compared in Table 3. The

values reported in this table for the most positive E_{10} indicate that the best catalytic activity corresponds to Pt/3Nb-TNT, followed by Pt/6Nb-TNT, Pt/6Nb-TiO_2 and Pt/3Nb-TiO_2, with E_{10} values of -0.024, 0.029, -0.032 and -0.034 V, respectively. These values are more positive than those corresponding to pristine TiO_2 and TNTs, which are of -0.038 and -0.042, also respectively.

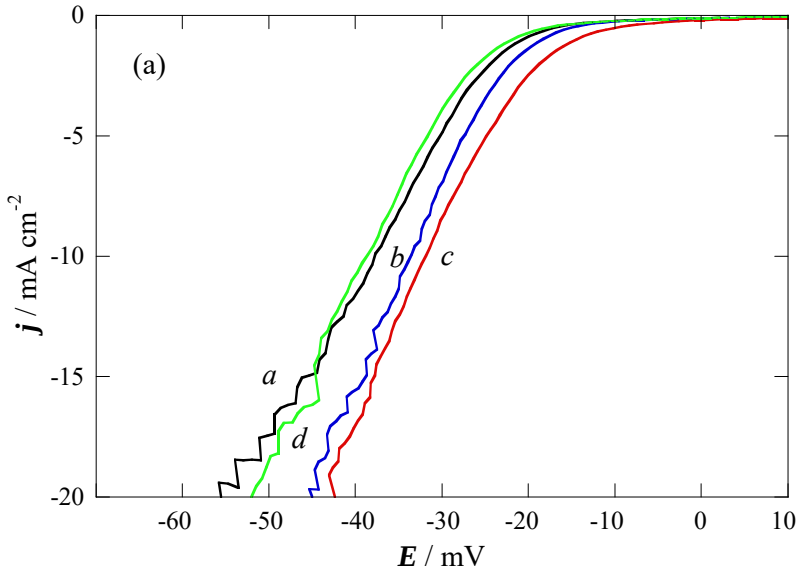

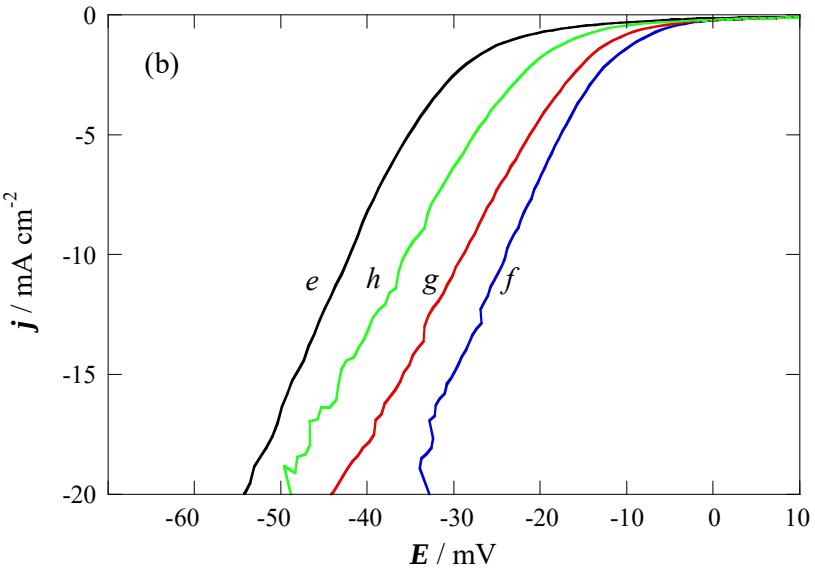

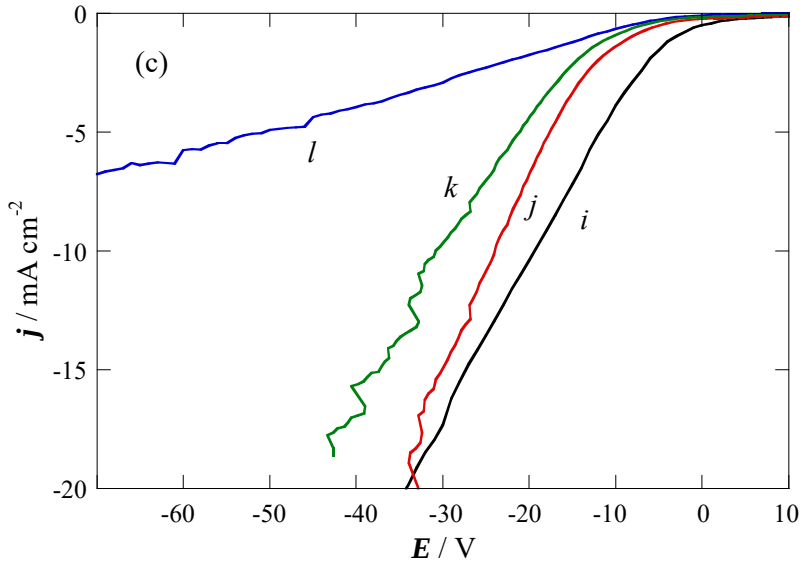

Fig. 8 – *j-E* curves corresponding to the HER in 0.50 mol dm^{-3} H_2SO_4 at 1 mV s^{-1} on 20 wt % Pt on (a) TiO_2-based, (b) TNTs-based supports and (c) comparison with commercial Pt/C. The different *j–E* curves correspond to (*a*) Pt/TiO_2, (*b*) Pt/3Nb-TiO_2, (*c*) Pt/6Nb-TiO_2, (*d*) Pt/10Nb-TiO_2, (*e*) Pt/TNTs, (*f*) Pt/3Nb-TNTs, (*g*) Pt/6Nb-TNTs, (*h*) Pt/10Nb-TNTs, (*i*) commercial Pt/C, (*j*) Pt/3Nb-TNT, (k) Pt/3Nb-TNT normalized to the ECSA and (l) commercial Pt/C normalized to the ECSA. *IR*-drop corrected. The current density has been referred to the electrode section except in curves (*k*) and (*l*).

It is interesting to compare the performance of the catalysts reported in this paper with published data relative to Pt deposited on other supports and to commercial carbon-supported Pt. This comparison is not straightforward because of the variety of Pt loadings and experimental conditions used to assess the HER catalyst activity. However, some comparisons can be established in terms of the E_{10} defined above (see Table 3), obtained from the LSV curves corrected by the ohmic drop, and Tafel slopes. Thus, Bhowmik et al [54] reported the HER on Pd-CN_x and commercial 10 wt % Pt/C in 0.50 M H_2SO_4. The E_{10} of the latter was about -0.058 V and the Tafel slope was 0.033 V dec^{-1}. Yang et al

[80] developed PtCo alloy nanoparticles encapsulated in carbon nanofibers for electrochemical hydrogen generation. From the reported *j-E* curves for HER in 0.50 M H_2SO_4, the E_{10} values obtained for PtCo/CNFs (5 wt % Pt) and Pt/CNF (8.5 wt % Pt) were -0.063 and -0.104 V, respectively. In the same work it was reported an E_{10} of about -0.057 V for commercial 20 wt. % Pt/C (Johnson-Matthey). Wang et al [40] developed monodisperse 20 wt. % Pt on N-doped black TiO_2 as high performance bifunctional catalyst. The E_{10} for the HER was about -0.035 V in 0.10 M H_2SO_4, reporting a Tafel slope of 0.033 V dec^{-1}. It was also shown an E_{10} value of 0.040 V for Pt/TiO_2 with a Tafel slope of 52 mV dec^{-1}, which is remarkably coincident with our results for Pt/TiO_2 and Pt/TNT, which are 0.040 ± 0.002 V. Zhang et al [81] synthesized a Pt/WS_2 (10 wt % Pt) catalyst for enhanced hydrogen evolution reaction. According to the experimental data, in N_2-saturated 0.50 M H_2SO_4, E_{10} was of -0.080 V with a Tafel slope of 0.055 V dec^{-1}. In the same paper, the same value of E_{10} of -0.080 V was given for Pt deposited on activated charcoal. It is also interesting to list the E_{10} value of -0.075 V for the Pt foil reported by Liu et al [43].

Due to the variety of the experimental conditions and the dispersion of values, the measurement of E_{10} was also performed for commercial Pt/C in the same conditions as those for the titania-supported catalysts. As indicated in Table 3 and shown in Fig. 8c, curve *i*, E_{10} was -0.020 V, which is more positive than that of Pt/3Nb-TNT (curve *j* in Fig. 8c). This value is closer to the value of -0.027 and -0.022 V reported recently for Pt/C and Pt-NCS [5]. However, the Pt/C catalyst used in this paper had higher ECSA than those of the titania-supported catalysts, 43 $m^2\ g_{Pt}^{-1}$ in front of 11-14 $m^2\ g_{Pt}^{-1}$, respectively. Therefore, the current densities referred to the ECSA should be more relevant to compare the catalysts activities. The corresponding figures were also plotted in Fig. 8c, curves *k* and *l*, for Pt/3Nb-TNT and Pt/C, respectively. It is apparent that when the current densities

are normalized to the ECSA, Pt/3Nb-TNT appears to be more active than Pt/C. These data strongly indicate the importance of the Pt support and confirm the good activity towards HER of Pt deposited on the TiO_2 and TNTs supports developed in this work. This good activity combined with its stability against corrosion by oxygen crossover, as shown by the oxygen evolution reaction studies on TiO_2 supports [29], makes Pt/Nb-TNT very promising as catalysts for the HER in PEMWEs. Although out of the scope of the present paper, stability tests are in perspective in real PEMWEs.

Table 3 – Electrode potential corresponding to a current density of 10 mA cm^{-2} in the steady linear sweep voltammograms (corrected by the *IR*-drop) of the HER in acidic media, 0.50 M H_2SO_4 unless otherwise indicated, on Pt deposited on different supports.

Electrocatalyst	**Pt content / wt %**	**Pt loading / µg cm^{-2}**	E_{10} **/ V**	**Reference**
Pt/TiO_2	20	14.0	-0.038	This work
$Pt/3Nb\text{-}TiO_2$	20	14.0	-0.034	Id.
$Pt/6Nb\text{-}TiO_2$	20	14.0	-0.032	Id.
$Pt/10Nb\text{-}TiO_2$	20	14.0	-0.039	Id.
Pt/TNT	20	14.0	-0.042	Id.
Pt/3Nb-TNT	20	14.0	-0.024	Id.
Pt/6Nb-TNT	20	14.0	-0.029	Id.
Pt/10Nb-TNT	20	14.0	-0.036	Id.
Pt/C (Premetek)	20	14.0	-0.020	Id.
Pt/C (Sigma-Aldrich)	10	42.0	-0.058	[54]
PtCo/CNF	5	15.7	-0.063	[80]
Pt/CNF	8.5	18.0	-0.104	[80]
Pt/C (Johnson-Matthey)	20	42.5	-0.057	[80]
Pt/TiO_2[a]	20	50.0	-0.040	[40]
$Pt/N_x\text{:}TiO_{2-x}$[a]	20	50.0	-0.035	[40]
Pt/WS_2	10	-[b]	-0.080	[81]
Pt/activated charcoal	10	-[b]	-0.080	[81]

Pt foil	100	-	-0.075	[43]
Pt/C	20	-[b]	-0.027	[5]
Pt-NCS[c]	-[b]	-[b]	-0.022	[5]
Pt-CS[d]	-[b]	-[b]	-0.041	[5]

[a] 0.10 M H_2SO_4.

[b] not reported.

[c] Pt nanoparticles embedded in N-enriched carbon matrix.

[d] Pt nanoparticles embedded in carbon matrix

The cathodic Tafel slope (b_c) has also been used as an indicative result of the catalytic activity, because in general, smaller Tafel slopes are obtained for catalysts with high charge transfer ability [40,54,82]. The generally established HER mechanism consists of an initial discharge step (1) followed by either an electrochemical desorption step (2) or a chemical recombination step (3). These steps are known as the Volmer, Heyrovsky and Tafel reactions, respectively, which can be written as follows:

$$H^+ + e^- \rightarrow H_{ads} \quad (1)$$

$$H_{ads} + H^+ + e^- \rightarrow H_2 \quad (2)$$

$$H_{ads} + H_{ads} \rightarrow H_2 \quad (3)$$

Depending on the rate-determining-step (rds), the values of b_c for Volmer, Heyrovsky and Tafel reactions are of 0.118, 0.040 and 0.029 V dec^{-1}, respectively [79].

Fig. 9a and b shows the E vs. log j plots for Pt deposited to 20 wt % on the Nb-doped TiO_2 and TNTs, respectively. As shown in this figure, values close to 0.030 V dec^{-1} were obtained for all the catalysts.

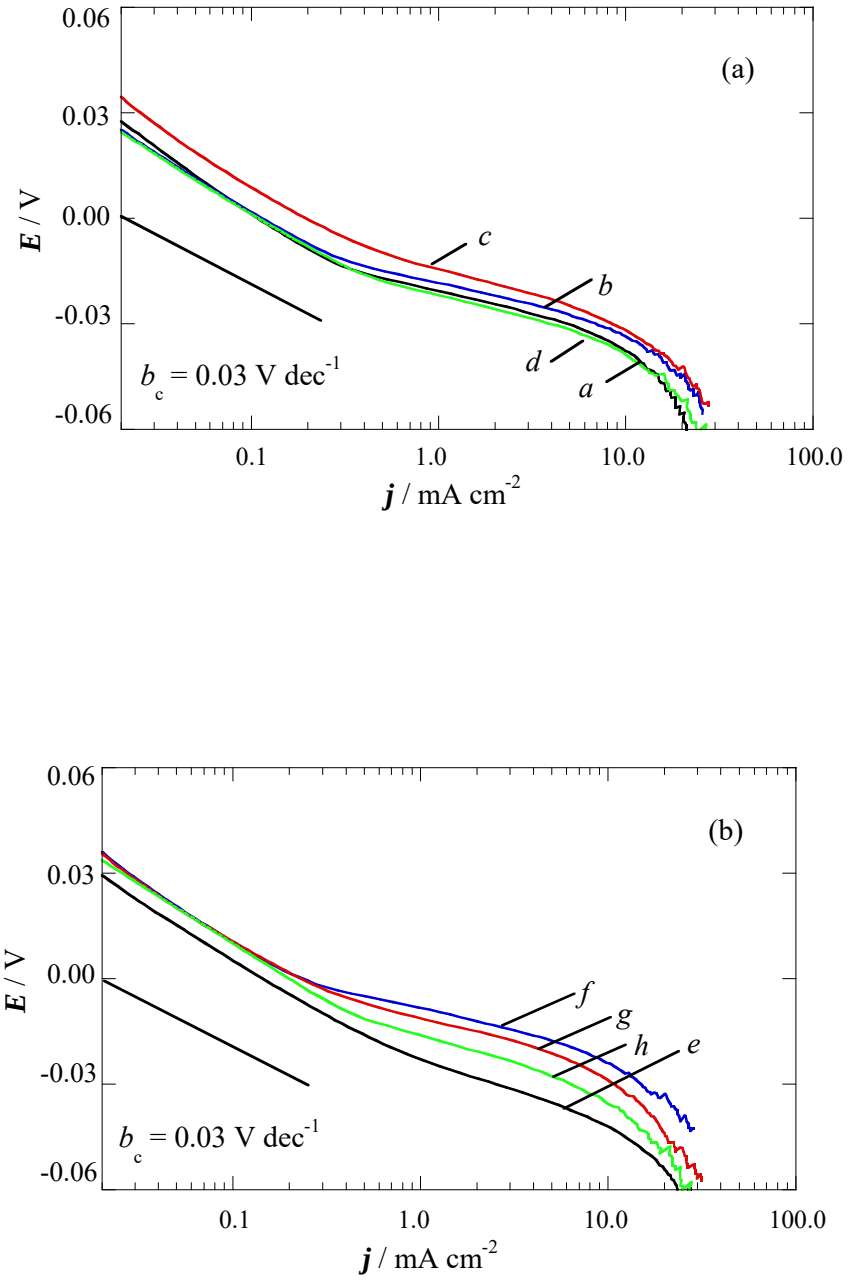

Fig. 9 –Tafel plots corresponding to the linear sweep voltammograms depicted in (a) Fig. 8a and (b) Fig. 8b. A Tafel slope of 0.03 V dec^{-1} has been drawn for comparison.

These values of the Tafel slopes indicate that the HER follows a Volmer-Tafel mechanism, the rds being the Tafel reaction, in agreement with previous results reported

in the literature for the HER on polycrystalline Pt-based catalysts [83]. It can be then suggested that the SMSI leading to a negative charge accumulation on Pt also facilitates the hydrogen desorption and therefore, it allows increasing the rate of the Tafel reaction.

4. Conclusions

Nb-doped TiO_2 and Nb-doped TNTs were synthesized and characterized to be used as supports of Pt nanoparticles for the HER electrocatalysis in water electrolysis. The specific surface areas of the Nb-doped TiO_2 support were in the range 87-100 m^2g^{-1}, whereas greater values of 260-303 m^2g^{-1} were achieved for Nb-doped TNTs. The presence of Nb increased the specific surface area of TiO_2 and TNTs. The lattice parameters, determined from XRD, showed the lattice expansion of titania with increasing the Nb doping. Also shown by the XRD results, the Pt nanoparticles deposited up to 20 wt % on the TiO_2 and TNTs supports had crystallite sizes of about 4-5 nm. The corresponding XPS analyses indicated a local increase of the electron density on Pt when supported on titania compared to Pt/C, which was attributed to the stronger interaction of Pt with the titania supports.

The electrochemical characterization towards HER in deaerated 0.50 mol dm^{-3} H_2SO_4 aqueous solution showed the good performance of the Pt electrocatalysts prepared with Nb-doped TiO_2 and TNTs supports, with higher catalytic activity per unit of electroactive surface area than that of commercial Pt/C. These results make the Pt/Nb-TNT catalysts, in particular that containing 3 at % Nb, very promising to be applied for the hydrogen evolution reaction in proton exchange membrane water electrolyzers.

Acknowledgements

This work was supported by the Initial Training Network, SUSHGEN, funded by the FP7 Marie Curie Actions of the European Commission (FP7-PEOPLE-ITN-2008-238678). The authors also thank to the Équipe AIME of the ICGM, UMR CNRS 5253, University of Montpellier II, for the physisorption study facilities.

References

[1] Carmo M, Fritz DL, Mergel J, Stolten D. A comprehensive review on PEM water electrolysis. Int J Hydrogen Energy 2013;38:4901–4934. https://doi-org.sire.ub.edu/10.1016/j.ijhydene.2013.01.151.

[2] Babic U, Suermann M, Büchi FN, Gubler L, Schmidt TJ. Review—identifying critical gaps for polymer electrolyte water electrolysis development. J Electrochem Soc 2017;164:F387–F399. http://dx.doi.org/10.1149/2.1441704jes.

[3] Kumar SS, Himabindu V. Hydrogen Production by PEM Water Electrolysis – A Review. Materials Science for Energy Technologies 2019. https://doi.org/10.1016/j.mset.2019.03.002.

[4] Qi J, Zhang W, Cao R. Solar-to-hydrogen energy conversion based on water splitting. Adv Energy Mater 2017;1701620. https://doi.org/10.1002/aenm.201701620.

[5] Jiang B, Yuan H, Dang Q, Wang T, Pang T, Cheng Y, Wu K, Wu X, Shao M. Quantitative evaluation of synergistic effects for Pt nanoparticles embedded in N-enriched carbon matrix as an efficient and durable catalyst for the hydrogen evolution reaction and their PEMWE performance. Int J Hydrogen Energy 2019;44:31121–31128. https://doi.org/10.1016/j.ijhydene.2019.10.036.

[6] Bernt M, Siebel A, Gasteiger HA. Analysis of voltage losses in PEM water electrolyzers with low platinum group metal loadings. J Electrochem Soc 2018;165: F305–F314. http://dx.doi.org/10.1149/2.0641805jes.

[7] Trasatti S. Work function, electronegativity, and electrochemical behaviour of metals: III. Electrolytic hydrogen evolution in acid solutions. J Electroanal Chem Interfacial Electrochem 1972;39:163–184. DOI: 10.1016/S0022-0728(72)80485-6.

[8] Shen W, Wu B, Liao F, Jiang B, Shao M. Optimizing the hydrogen evolution reaction by shrinking Pt amount in Pt-Ag/SiNW nanocomposites. Int J Hydrogen Energy 2017;42:15024–15030. https://doi.org/10.1016/j.ijhydene.2017.03.110

[9] Nguyen HD, Nguyen TTL, Nguyen KM, Ha TH, Nguyen QH. Preparation of the Vulcan XC72R-supported Pt nanoparticles for the hydrogen evolution reaction in PEM water electrolysers. Adv Nat Sci: Nanosci Nanotechnol 2015;6:025012–025017. https://doi.org/10.1088/2043-6262/6/2/025012.

[10] Eftekhari, A. Electrocatalysts for hydrogen evolution reaction. Int J Hydrogen Energy 2017;42:11053–11077. https://doi.org/10.1016/j.ijhydene.2017.02.125.

[11] Grigoriev SA, Millet P, Fateev VN. Evaluation of carbon-supported Pt and Pd nanoparticles for the hydrogen evolution reaction in PEM water electrolysers. J Power Sources 2008;177:281–285. https://doi-org.sire.ub.edu/10.1016/j.jpowsour.2007.11.072.

[12] Kumar ETD, Ganesh V. Hierarchically ordered tubular titanium dioxide electrodes: preparation, electrochemical characterization, and application as a bifunctional catalyst. ChemElectroChem 2014;1:590–600. https://doi-org.sire.ub.edu/10.1002/celc.201300132.

[13] Li T, Tang Z, Wang K, Wu W, Chen S, Wang C. Palladium nanoparticles grown on β-Mo_2C nanotubes as dual functional electrocatalysts for both oxygen reduction reaction

and hydrogen evolution reaction. Int J Hydrogen Energy 2018;43:4932–4941. https://doi.org/10.1016/j.ijhydene.2018.01.107.

[14] Price E. Durability and Degradation Issues in PEM Electrolysis Cells and its Components. The second international workshop organised by the NOVEL EU-funded programme. Johnson Matthey Technol. Rev. 2017;61:47-51. https://doi.org/10.1595/205651317X693732.

[15] Trinke P, Bensmann B, Hanle-Rauschenbach R. Experimental evidence of increasing oxygen crossover with increasing current density during PEM water electrolysis. Electrochem Commun 2017;82:98-102. https://doi.org/10.1016/j.elecom.2017.07.018.

[16] Chandesris M, Médeau V, Guillet N, Chelghoum S, Thoby D, Fouda-Onana F. Membrane degradation in PEM water electrolyzer: Numerical modeling and experimental evidence of the influence of temperature and current density. Int J Hydrogen Energy 2015;40:1353–1366. http://dx.doi.org/10.1016/j.ijhydene.2014.11.111.

[17] Nah Y-C, Paramasivam I, Schmuki P. Doped TiO_2 and TiO_2 nanotubes: Synthesis and applications. Chem Phys Chem 2010;11:2698–2713. https://doi-org.sire.ub.edu/10.1002/cphc.201000276.

[18] Chen X, Mao SS. Titanium Dioxide Nanomaterials: Synthesis, Properties, Modifications, and Applications. Chem Rev 2007;107:2891–2959. https://doi-org.sire.ub.edu/10.1021/cr0500535.

[19] Ruiz A, Dezanneau G, Arbiol J, Cornet A, Morante JR. Study of the influence of Nb content and sintering temperature on TiO_2 sensing films. Thin Solid Films 2003;436:90–94. https://doi-org.sire.ub.edu/10.1016/S0040-6090(03)00515-7.

[20] Kim JY, Sekino T, Tanaka SI. Influence of the size-controlled TiO_2 nanotubes fabricated by low-temperature chemical synthesis on the dye-sensitized solar cell properties. J Mater Sci 2011;46:1749–1757. DOI: 10.1007/s10853-010-4994-2.

[21] Xu X, Guo Y, Liang Z, Cui H, Tian J. Remarkable charge separation and photocatalytic efficiency enhancement through TiO_2(B)/anatase hetrophase junctions of TiO_2 nanobelts. Int J Hydrogen Energy 2019;44:27311–27318. https://doi.org/10.1016/j.ijhydene.2019.08.174.

[22] Mozia S, Borowiak-Paleń E, Przepiórski J, Grzmil B, Tsumura T, Toyoda M, Grzechulska-Damszel J, Morawski AW. Physico-chemical properties and possible photocatalytic applications of titanate nanotubes synthesized via hydrothermal method. J Phys Chem Solids 2010;71:263–272. https://doi-org.sire.ub.edu/10.1016/j.jpcs.2009.12.074.

[23] Fu Y, Wei ZD, Chen SG, Li L, Feng YC, Wang YQ, Ma XL, Liao MJ, Shen PK, Jiang SP. Synthesis of Pd/TiO_2 nanotubes/Ti foil for oxygen reduction reaction in acidic solution. J Power Sources 2009;189:982–987. https://doi-org.sire.ub.edu/10.1016/j.jpowsour.2008.12.065.

[24] Shim J, Lee CR, Lee HK, Lee JS, Cairns EJ. Electrochemical characteristics of Pt-WO_3/C and Pt-TiO_2/C electrocatalysts in a polymer electrolyte fuel cell. J Power Sources 2001;102:172–177. https://doi-org.sire.ub.edu/10.1016/S0378-7753(01)00817-5.

[25] Xiong L, Manthiram A. Synthesis and characterization of methanol tolerant Pt/TiO_x/C nanocomposites for oxygen reduction in direct methanol fuel cells. Electrochim Acta 2004;49:4163–4170. https://doi-org.sire.ub.edu/10.1016/j.electacta.2004.04.011.

[26] Gustavsson M, Ekström H, Hanarp P, Eurenius L, Lindbergh G, Olsson E, Kasemo B. Thin film Pt/TiO_2 catalysts for the polymer electrolyte fuel cell. J Power Sources 2007;163:671–678. https://doi-org.sire.ub.edu/10.1016/j.jpowsour.2006.10.005.

[27] Lewera A, Timperman L, Roguska A, Alonso-Vante N. Metal support interactions between nanosized Pt and metal oxides (WO_3 and TiO_2) studied using X-ray photoelectron spectroscopy. J Phys Chem C 2011;115:20153–20159. https://doi-org.sire.ub.edu/10.1021/jp2068446.

[28] Mazúr P, Polonský J, Paidar M, Bouzek K. Non-conductive TiO_2 as the anode catalyst support for PEM water electrolysis. Int J Hydrogen Energy 2012;37:12081–12088. https://doi-org.sire.ub.edu/10.1016/j.ijhydene.2012.05.129.

[29] Hao C, Lv H, Mi C, Song Y, Ma J. Investigation of mesoporous niobium-doped TiO_2 as an oxygen evolution catalyst support in an SPE water electrolyzer. ACS Sustainable Chem Eng 2016;4:746–756. https://doi-org.sire.ub.edu/10.1021/acssuschemeng.5b00531.

[30] Chhina H, Campbell S, Kesler O. Ex Situ and In Situ stability of Platinum supported on Niobium–doped titania for PEMFCs. J Electrochem Soc 2009;156:B1232–B1237. DOI: 10.1149/1.3184155.

[31] Trenczek-Zając A, Rekas M. Electrical Properties of Nb-doped titanium dioxide TiO_2 at room temperature. Mater Sci Poland 2006;24:53–60. https://www.researchgate.net/publication/282507820.

[32] Sotter E, Vilanova X, Llobet E, Stankova M, Correig X. Niobium–doped titania nanopowders for gas sensor applications. J Optoel Adv Mater 2005;7:1395–1398. https://www.researchgate.net/publication/266422066.

[33] Elezović NR, Babić BM, Gajić-Krstajić L, Radmilović V, Krstajić NV, Vračar LJ. Synthesis, characterization and electrocatalytical behavior of Nb-TiO_2/Pt nanocatalyst for

oxygen reduction reaction. J Power Sources 2010;195:3961–3968. https://doi-org.sire.ub.edu/10.1016/j.jpowsour.2010.01.035.

[34] Gojković SL, Babić BM, Radmilović VR, Krstajić VN. Nb-doped TiO_2 as a support of Pt and Pt-Ru anode catalyst for PEMFCs. J Electroanal Chem 2010;639:161–166. https://doi-org.sire.ub.edu/10.1016/j.jelechem.2009.12.004.

[35] Morgan BJ, Scanlon DO, Watson GW. Small polarons in Nb- and Ta-doped rutile and anatase TiO_2. J Mater Chem 2009;19:5175–5178. http://dx.doi.org/10.1039/B905028K.

[36] Do TB, Cai M, Ruthkosky MS, Moylan TE. Niobium–doped titanium dioxide for fuel cell application. Electrochim Acta 2010;55:8013–8017. https://doi-org.sire.ub.edu/10.1016/j.electacta.2010.03.027.

[37] Chevallier L, Bauer A, Cavaliere S, Hui R, Rozière J, Jones DJ. Mesoporous nanostructured Nb-Doped titanium dioxide microsphere catalyst supports for PEM fuel cell electrodes. Appl Mater Interfaces 2012;4:1752−1759. https://doi-org.sire.ub.edu/10.1021/am300002j.

[38] Hu W, Chen S, Xia Q. IrO_2/Nb-TiO_2 electrocatalyst for oxygen evolution reaction in acidic medium. Int J Hydrogen Energy 2014;39:6967–6976. https://doi-org.sire.ub.edu/10.1016/j.ijhydene.2014.02.114.

[39] Genova-Koleva RV, Alcaide F, Álvarez G, Cabot PL, Grande HJ, Martínez-Huerta MV, Miguel O. Supporting IrO_2 and $IrRuO_x$ nanoparticles on TiO_2 and Nb-doped TiO_2 nanotubes as electrocatalysts for the oxygen evolution reaction. J Energy Chem 2019;34:227–239. https://doi.org/10.1016/j.jechem.2019.03.018.

[40] Wang X, Yuan X, Liu X, Dong W, Dong C, Lou M, Li J, Lin T, Huang F. Monodisperse Pt nanoparticles anchored on N-doped black TiO_2 as high performance

bifunctional electrocatalyst. J Alloy Compd 2017;701:689–675. https://doi.org/10.1016/j.jallcom.2017.01.152.

[41] Lacnjevac UC, Radmilovic VV, Radmilovic VR, Krstajic NV. RuO_x nanoparticles deposited on TiO_2 nanotube arrays by ion-exchange method as electrocatalysts for the hydrogen evolution reaction in acid solution. Electrochim Acta 2015;168:178–190. http://dx.doi.org/10.1016/j.electacta.2015.04.012.

[42] Gao S, Wang B, Liu X, Guo Z, Liu Z, Wang Y. PbTe quantum dots as electron transfer intermediates for the enhanced hydrogen evolution reaction of amorphous MoS_x/TiO_2 nanotube arrays. Nanoscale 2018;10:10288. DOI: 10.1039/c8nr02532k.

[43] Liu Z, Zhang X, Wang B, Xia M, Gao S, Liu X, Zavabeti A, Ou JZ, Kalantar-Zadeh K, Wang Y. Amorphous MoS_x-coated TiO_2 nanotube arrays for enhanced electrocatalytic hydrogen evolution reaction. J Phys Chem C 2018;122:12589−12597. DOI: 10.1021/acs.jpcc.8b01678.

[44] Wei Y, Fu J, Song H, Zhang B, Pi C, Xia L, Zhang X, Gao B, Zheng Y, Chu PK. N-doped TiO_2 nanotube arrays with uniformly embedded Co_xP nanoparticles for high-efficiency hydrogen evolution reaction. RSC Advances 2019;9:11676-11682. DOI: 10.1039/C9RA01184F.

[45] Li Y, Yang P, Wang B, Liu Z. Amorphous Ni_xCo_yP-supported TiO_2 nanotube arrays as an efficient hydrogen evolution reaction electrocatalyst in acidic solution. Beilstein J Nanotechnol 2019;10:62–70. DOI:10.3762/bjnano.10.6.

[46] Yuan M, Zhu Y, Deng L, Ming R, Zhang A, Li W, Chai B, Ren Z. IrO_2–TiO_2 electrocatalysts for the hydrogen evolution reaction in acidic water electrolysis without activation. New J Chem 2017;41:6152-6159. DOI: 10.1039/c7nj00756f.

[47] Yu J, Zhou W, Xiong T, Wang A, Chen S, Chu B. Enhanced electrocatalytic activity of Co@N-doped carbon nanotubes by ultrasmall defect-rich TiO_2 nanoparticles for

hydrogen evolution reaction. Nano Res 2017;10:2599–2609. DOI 10.1007/s12274-017-1462-1.

[48] Li M, Liu H, Song Y, Li Z. TiO_2 homojunction with Au nanoparticles decorating as an efficient and stable electrocatalyst for hydrogen evolution reaction. Materials Characterization 2019;151:286–291. https://doi.org/10.1016/j.matchar.2019.03.025.

[49] Tahira A, Ibupoto ZH, Mazzaro R, You S, Morandi V, Natile MM, Vagin M, Vomiero A. Advanced electrocatalysts for hydrogen evolution reaction based on core−shell MoS_2/TiO_2 nanostructures in acidic and alkaline media. ACS Appl Energy Mater 2019;2:2053-2062. DOI: 10.1021/acsaem.8b02119.

[50] Wang K, Chen Q, Hu Y, Wei W, Wang S, Shen Q, Qu P. Crystalline $Ru_{0.33}Se$ nanoparticles-decorated TiO_2 nanotube arrays for enhanced hydrogen evolution reaction. Small 2018;14:1802132. https://doi.org/10.1002/smll.201802132.

[51] Nong S, Dong W, Yin J, Dong B, Lu Y, Yuan X, Wang X, Bu K, Chen M, Jiang S, Liu LM, Sui M, Huang F. Well-dispersed ruthenium in mesoporous crystal TiO_2 as an advanced electrocatalyst for hydrogen evolution reaction. J Am Chem Soc 2018;140:5719−5727. DOI: 10.1021/jacs.7b13736.

[52] Franceschini EA, Gomez MJ, Lacconi GI. One step synthesis of high efficiency nickel/mesoporous TiO_2 hybrid catalyst for hydrogen evolution reaction. J Energy Chem 2019;29:79–87. https://doi.org/10.1016/j.jechem.2018.02.005.

[53] Zhang Y, Bilan HK, Podlaha E. Enhancing the hydrogen evolution reaction with Ni-W-TiO_2 composites. Electrochem Commun 2018;96:108–112. https://doi.org/10.1016/j.elecom.2018.10.015

[54] Bhowmik T, Kundu MK, Barman S. Palladium nanoparticle–graphitic carbon nitride porous synergistic catalyst for hydrogen evolution/oxidation reactions over a broad range

of pH and correlation of its catalytic activity with measured hydrogen binding energy. ACS Catal 2016;6:1929–1941. https://doi-org.sire.ub.edu/10.1021/acscatal.5b02485.

[55] Tighineanu A, Ruff T, Albu S, Hahn R, Schmuki P. Conductivity of TiO_2 nanotubes: Influence of annealing time and temperature. Chem Phys Lett 2010;494:260–263. https://doi-org.sire.ub.edu/10.1016/j.cplett.2010.06.022.

[56] Kasuga T, Hiramatsu M, Hoson A, Sekino T, Niihara K. Formation of titanium oxide nanotube. Langmuir 1998;14:3160–3163. https://doi-org.sire.ub.edu/10.1021/la9713816.

[57] Ma Y, Lin Y, Xiao X, Zhou X, Li X. Sonication–hydrothermal combination technique for the synthesis of titanate nanotubes from commercially available precursors. Mater Res Bull 2006;41:237–243. https://doi.org/10.1016/j.materresbull.2005.08.020.

[58] Milanović M, Nikolić LM, Stijepović I, Kontos AG, Giannakopoulos KP. Steps in growth of Nb-doped layered titanates with very high surface area suitable for water purification. Mater Chem Phys 2014;148:874-881. https://doi.org/10.1016/j.matchemphys.2014.08.064.

[59] Wada E, Kitano M, Yamamoto K, Nakajima K, Hayashi S, Hara M. Synthesis of niobium-doped titanate nanotubes as solid acid catalysts. Catal Sci Technol 2016;6:4832-4839. DOI: 10.1039/c6cy00044d.

[60] Bavykin DV, Parmon VN, Lapkin AA, Walsh FC. The effect of hydrothermal conditions on the mesoporous structure of TiO_2 nanotubes. J Mater Chem 2004;14:3370–3377. https://doi-org.sire.ub.edu/10.1039/B406378C.

[61] Kasuga T. Formation of titanium oxide nanotubes using treatments and their characteristic properties. Thin Solid Films 2006;496:141–145. https://doi-org.sire.ub.edu/10.1016/j.tsf.2005.08.341.

[62] Ou HH, Lo SL. Review of titania nanotubes synthesized via the hydrothermal treatment: Fabrication, modification, and application. Sep Purif Technol 2007;58:179–191. https://doi.org/10.1016/j.seppur.2007.07.017.

[63] Xu Y, Xie X, Guo J, Wang S, Wang Y, Mathur VK. Effects of annealing treatment and pH on preparation of citrate-stabilized PtRu/C catalyst. J Power Sources 2006;162:132–140. https://doi.org/10.1016/j.jpowsour.2006.07.021.

[64] Pantea D, Darmstadt H, Kaliaguine S, Roy C. Electrical conductivity of conductive carbon blacks: influence of surface chemistry and topology. Appl Surf Sci 2003;217:181-193. https://doi.org/10.1016/S0169-4332(03)00550-6.

[65] Pérez-Rodríguez S, Pastor E, Lázaro MJ. Electrochemical behavior of the carbon blackVulcan XC-72R: Influence of the surface chemistry. Int J Hydrogen Energy 2018;43:7911-7922. https://doi.org/10.1016/j.ijhydene.2018.03.0400360-3199.

[66] Weibel A, Bouchet R, Boulc'h F, Knauth P. The big problem of small particles: a comparison of methods for determination of particle size in nanocrystalline anatase powders. Chem Mater 2005;17:237–2385. https://doi-org.sire.ub.edu/10.1021/cm0403762.

[67] Nart FC, Vielstich W. Normalization of porous active surfaces. In Vielstich W, Lamm A, Gasteiger HA, editors. Handbook of fuel cells. Fundamentals; technology and applications, vol. 2, Chichester: John Wiley & Sons; 2003, p. 302–315.

[68] Yuan ZY, Su BL. Titanium oxide nanotubes, nanofibers and nanowires. Colloids and Surfaces A: Physicochem. Eng. Aspects 2004;241:173-183. https://doi.org/10.1016/j.colsurfa.2004.04.030.

[69] Chu S-Y, Chen T-Y, Tsai I-T, Water W. Doping effects of Nb additives on the piezoelectric and dielectric properties of PZT ceramics and its application on SAW

device. Sensor Actuat A-Phys 2004;113:198–203. https://doi-org.sire.ub.edu/10.1016/j.sna.2004.02.020.

[70] Chhina H, Campbell S, Kesler O. Characterization of Nb and W doped titania as catalyst supports for Proton Exchange Membrane Fuel Cells. J New Mater Electrochem Syst 2009;12:177–185. https://www.researchgate.net/publication/279565609.

[71] Rau S, Colom Tomás J, Smolinka T, Fuentes RE, Weidner, JW. PEM electrolyzer with nano-structured electrodes for high efficient hydrogen production. In: Stolten D, Grube T, editors. Parallel Sessions book 3: hydrogen production technologies – part 2: Proceedings of the WHEC; 2010 May 16-21; Essen, Germany. Jülich: Verlag; 2010. p. 151-156.

[72] Bagheri S, Julkapli NM, Hamid SBA. Titanium dioxide as a catalyst support in heterogeneous catalysis. Sci World J. 2014;727496. http://dx.doi.org/10.1155/2014/727496.

[73] Moulder JF, Stickle WF, Sobol PE, Bomben KD. Handbook of X-ray Photoelectron Spectroscopy. A reference book of standard spectra for identification and interpretation of XPS data. Eden Prairie, MN: Perkin-Elmer Corp, Physical Electronics; 1995.

[74]. Maya-Cornejo J, Carrera-Cerritos R, Sebastián D, Ledesma-García J, Arriaga LG, Aricò AS, Baglio V. PtCu catalyst for the electro-oxidation of ethanol in an alkaline direct alcohol fuel cell. Int J Hydrogen Energy 2017;42:27919–27928. https://dx.doi.org/10.1016/j.ijhydene.2017.07.226.

[75] Liu Y, Szeifert JM, Feckl JM, Mandlmeier B, Rathousky J, Hayden O, Fattakhova-Rohlfing D, Bein T. Niobium-Doped Titania Nanoparticles: Synthesis and Assembly into Mesoporous Films and Electrical Conductivity. ACS Nano 2010;4:5373–5381. https://pubs.acs.org/doi/10.1021/nn100785j.

[76] Esparbé I, Brillas E, Centellas F, Garrido JA, Rodríguez RM, Arias C, Cabot PL. Structure and electrocatalytic performance of carbon-supported platinum nanoparticles. J Power Sources 2009;190:201-209. https://doi.org/10.1016/j.jpowsour.2009.01.075.

[77] Angerstein-Kozlowska H. Surfaces, cells, and solutions for kinetic studies. In: Yeager E, Bockris JO'M, Conway BE, Sarangapani S, editors. Comprehensive Treatise of Electrochemistry, vol. 9, New York: Plenum Press; 1984, p. 15–59.

[78] Wang J, Xu F, Jin H, Chen Y, Wang Y. Non-noble metal-based carbon composites in hydrogen evolution reaction: fundamentals to applications. Adv Mat 2017;29:1605838. https://doi-org.sire.ub.edu/10.1002/adma.201605838.

[79] Anantharaj S, Ede SR, Sakthikumar K, Karthick K, Mishra S, Kundu S. Recent trends and perspectives in electrochemical water splitting with an emphasis on sulfide, selenide, and phosphide catalysts of Fe, Co, and Ni: A Review. ACS Catal 2016;6:8069–8097. https://doi-org.sire.ub.edu/10.1021/acscatal.6b02479.

[80] Yang TT, Zhu H, Wan M, Dong L, Zhang M, Du ML. Highly efficient and durable PtCo alloy nanoparticles encapsulated in carbon nanofibers for electrochemical hydrogen generation. Chem Comm 2016;52:990–993. DOI: 10.1039/c5cc08097e.

[81] Zhang Y, Yan J, Ren X, Pang L, Chen H, Liu S. 2D WS_2 nanosheet supported Pt nanoparticles for enhanced hydrogen evolution reaction. Int J Hydrogen Energy 2017;42:5472–5477. http://dx.doi.org/10.1016/j.ijhydene.2016.08.225.

[82] Uosaki K, Elumalai G, Dinh HC, Lyalin A, Taketsugu T, Noguchi H. Highly efficient electrochemical hydrogen evolution reaction at insulating boron nitride nanosheet on inert gold substrate Sci Rep 2016;6:32217. DOI: 10.1038/srep32217.

[83] Lasia A. Hydrogen evolution reaction. In Vielstich W, Lamm A, Gasteiger HA editors. Handbook of fuel cells. Fundamentals; technology and applications, vol. 2, Chichester: John Wiley & Sons; 2003, p. 416–440.